FINAL TECHNICAL REPORT

USGS NEHRP AWARD #08HQGR0040

SEISMOTECTONICS OF THE NEW MADRID SEISMIC ZONE: IMPROVED VELOCITY MODELS AND FAULT CHARACTERIZATION

Christine Powell

Stephen Horton

Center for Earthquake Research and Information

University of Memphis

3876 Central Ave. Suite 1

Memphis, TN 38152-3050

Telephone: (901) 678-8455

Fax: (901) 678-4734

Email: capowell@memphis.edu

December 23, 2009

USGS NEHRP AWARD #08HQGR0040, *SEISMOTECTONICS OF THE NEW MADRID SEISMIC ZONE: IMPROVED VELOCITY MODELS AND FAULT CHARACTERIZATION* by Christine Powell and Stephen Horton, Center for Earthquake Research and Information, University of Memphis, 3876 Central Ave., Suite 1, Memphis, TN 38152- 3050. Telephone: (901) 678-8455, Fax:(901) 678-4734, Email: capowell@memphis.edu

ABSTRACT

High resolution earthquake relocations and velocity models are calculated for the New Madrid Seismic Zone (NMSZ) using the double-difference algorithm. We construct three-dimensional P and S wave velocity models for the NMSZ using double difference local earthquake tomography (tomoDD). TomoDD incorporates catalog arrival times with catalog and WCC differential times to solve for P and S wave velocity structure and for high-resolution earthquake locations. The data set consists of a combination of travel times and differential times recorded by the CNMSN from 2000-2007 and the temporary Portable Array for Numerical Data Acquisition (PANDA) deployment from 1989-1992. A total of 4522 P wave arrivals and 3953 S wave arrivals result in 18662 P wave differential times and 16354 S wave differential times for the PANDA deployment. We use 15146 P wave and 10387 S wave arrivals resulting in 63321 P wave differential times and 37187 S wave differential times from 837 earthquakes recorded by the CNMSN. Additionally, 37040 P wave and 18731 S wave WCC times strengthen the inversion results. We use a finite difference travel time calculator combined with an irregular inversion grid of nodes spaced every 5 to 20 km horizontally and 1 to 3 km vertically. Model resolution is examined using checkerboard synthetic tests and indicates that resolution is highest close to the source region between depths of 5 to 11 km. P wave velocities are close to the source region are low relative to the 1D starting velocity model. S wave velocities are relatively high in the northern portion of the NMSZ, resulting in low Vp/Vs ratios, and relatively low in the southern portion. A major strike-slip arm of seismicity, the Cottonwood Grove – Blytheville arch (CG-BA) fault, trends NE-SW and separates relatively high P and S wave velocities to the NW from relatively low velocities to the SE. This fault could be a reactivation of an ancient basement feature. We suggest that the low P and S wave velocities associated with the southern portion of the Reelfoot fault, the major reverse fault in the NMSZ, are caused by highly fractured, fluid filled rocks. This portion of the Reelfoot fault is also the location of earthquake swarm activity. We also image the mafic Malden pluton located in the NW corner of the NMSZ.

We also investigate the effects of the thick, low-velocity, unconsolidated Mississippi Embayment sediments on local earthquake tomography using a priori information regarding sediment thickness and velocities. We show that the unconsolidated sediments do not exert a first-order effect on the tomography results. Finally, we invert CNMSN and PANDA P and S wave arrival time data using a tomographic algorithm that differs from tomoDD. We perform a simultaneous inversion for P and S wave velocities and hypocentral locations. The inversion algorithm uses blocks rather than grid nodes and differential times are not utilized. Joint 3-D velocity inversion results are very similar to the tomoDD solution when the block size is equivalent to the smallest node spacing (5 km); the same major velocity anomalies are resolved in both solutions. Reducing the

block size to 2x2x2 km yields detailed images of the upper portion of the crust near the major arms of seismicity.

SCIENTIFIC INVESTIGATIONS

Introduction

The New Madrid seismic zone (NMSZ) has been the subject of numerous geophysical investigations because it presents an enigma; the zone consists of several, well-defined branches of seismicity but is located in the center of a tectonic plate, hundreds of kilometers from an active plate boundary (Figure 1). The NMSZ generated at least three earthquakes in 1811-1812 exceeding moment magnitude 7.0 (Johnston and Schweig, 1996; Hough et al., 2000) and paleoseismology indicates that at least five episodes of large earthquakes capable of producing wide-spread liquefaction occurred in the NMSZ over the past 5000 years (Tuttle, 2001; Tuttle et al., 2005). Recently, the NMSZ has been the focal point of scientific controversy primarily centered on the interpretation of GPS strain rate calculations. GPS studies have shown that strain rates in the NMSZ may be much smaller than rates along the San Andreas fault system at the plate boundary; this has been used as evidence that NMSZ earthquake hazards have been overestimated (Calais et al., 2005; Newman et al., 1999; Stein, 2007). However, other GPS measurements indicate that significant strain is accumulating across the Reelfoot fault within the NMSZ (Smalley et al., 2005). Differences in GPS interpretations are related to fundamental unknowns in how monument drift errors are estimated. Arguments based upon the GPS data can be made that the NMSZ is becoming inactive, based on plate boundary fault models (Stein, 2007), or that future large earthquakes are a virtual certainty, based on the behavior of plate interior viscoelastic oscillator models (Kenner and Segall, 2000). Adding to the controversy is a geodynamic model constructed from mantle tomography results. According to this model, the subducting Farallon plate deep under central North America is inducing mantle flow that is depressing New Madrid lithosphere and producing long-term compressional stresses that drive earthquake activity in the seismic zone (Forte et al., 2007). The paleoseismic evidence, the continuous occurrence of earthquakes in the seismic zone, possible GPS strain signals, the variety of geodynamic models that may relate to earthquake genesis, and recent geological history all indicate that it is premature to assume that the NMSZ will never generate another large earthquake. Continued investigation of the seismic zone is compelling from a hazards perspective and because the NMSZ is one of the great unsolved scientific mysteries of North American geology.

The NMSZ is buried beneath hundreds of meters of unconsolidated Mississippi Embayment sediments but active faults can be identified by the occurrence of microseismicity along distinct bands (Figure 1). Two of these are associated with named faults that likely failed in the 1811-1812 earthquake sequence. The Cottonwood Grove – Blytheville Arch (CG-BA) fault extends in a NE-SW orientation along the central Reelfoot rift (Russ, 1982). Motion along this fault and other NE-SW trending faults, is primarily dextral strike-slip. The Reelfoot fault extends NW-SE across the Mississippi River (Russ, 1982), and reverse motion along this fault is thought to have resulted in the formation of Reelfoot Lake and changing flow within the Mississippi River during the 1811-1812 earthquake sequence. Commonly, the Reelfoot fault is divided into two segments, one north of the intersection of the CG-BA fault and one south of this juncture.

Fault orientation within the NMSZ is consistent with the present-day regional stress field in the central US, with maximum compressional stress oriented E-W.

In this study, we provide detailed, three-dimensional Vp and Vs images for the NMSZ and a set of high-resolution, relocated hypocenters. The velocity images provide insight into the seismotectonic framework of the zone and material properties of the seismogenic crust. Our approach is two-fold. The first step involves construction of three-dimensional P and S wave velocity models for the NMSZ using double difference local earthquake tomography (tomoDD). As a second step, we determine the effects of the thick, unconsolidated Embayment sediments on local earthquake tomography using several approaches and then invert for P and S wave velocities and hypocentral locations using a tomographic algorithm that differs significantly in its methodology from tomoDD. Due to the size restriction imposed on this report, we will show only those figures that best demonstrate conclusions drawn. Other figures including those containing resolution results, can be found in the dissertation and three publications that result from this study.

Geologic Setting

The most widely accepted tectonic model for the NMSZ host structure is an intracratonic graben formed in latest Precambrian to early Cambrian times (Thomas, 1991). Faulted Precambrian basement rocks and Paleozoic sedimentary rocks are overlain unconformably by Mesozoic and Cenozoic rocks of the Mississippi Embayment. Strongest evidence for the graben, called the Reelfoot rift, is provided by gravity and magnetic data (Hildenbrand, 1985); the rift is characterized by a northeast trending, approximately 70 km wide zone of subdued aeromagnetic anomalies and corresponding gravity lows. There is no evidence from potential field data or radiometric dating of well samples that mafic magma intruded the graben during the initial rifting stage. Gravity and magnetic data indicate the presence of shallow mafic intrusions along the border faults (Figure 1); these intrusions were emplaced during a reactivation of the rift, probably in late Cretaceous time (Hildenbrand, 1985). There is some evidence provided by gravity and seismic refraction data that the Reelfoot rift is underlain by anomalously dense upper mantle/lower crust (Ervin and McGinnis, 1975; Mooney et al., 1983; Catchings, 1999). The Reelfoot rift appears to be a feature that represents limited extension in the shallow crust but one that has been reactivated in both extensional and compressional modes.

Precambrian basement rocks below the Reelfoot rift are buried beneath Phanerozoic sediments but regional mapping indicates that the rift and surrounding region are underlain by the Precambrian Eastern Granite-Rhyolite Province (1470 ± 30 Ma) and the Southern Granite-Rhyolite Province (1370 ± 30 Ma). The NMSZ lies entirely within the Eastern Granite-Rhyolite Province (van der Pluijm and Catacosinos, 1996). Hildenbrand et al. (1996) suggest that the Late Precambrian Missouri batholith extends under the NMSZ based upon interpretation of gravity and magnetic data. Proterozoic rocks of the Reelfoot rift region consist primarily of granite, granite porphyry, and dioritic gneiss as determined from drill cores (Thomas, 1985; Dart, 1992; Dart and Swolfs, 1998). Rocks of similar age in the Eastern Granite-Rhyolite Province are exposed in the nearby St. Francois Mountains in southeastern Missouri (Thomas, 1985; Dart and Swolfs, 1998).

During rifting, local erosion of nearby granite rocks provided Early Cambrian basal arkosic sediments within the Reelfoot rift (Crone et al., 1985; Dart and Swolfs, 1998). After Middle Cambrian time, deposition within the rift shifted from subaerial to marine and as much as 6 km of marine Upper Cambrian Lamotte Sandstone, Bonterre Formation limestones, Elvins Group shales, and the Potsdam Supergroup were deposited (Thomas, 1985; Howe and Thompson, 1984). Deposition kept pace with regional subsidence during Late Cambrian–Middle Ordovician time (Howe and Thompson, 1984; Howe et al., 1984; Dart and Swolfs, 1998), resulting in the thick, shallow marine Knox (Arbuckle) carbonate Supergroup that overlies the rift (Thomas, 1985; Howe and Thompson, 1984). Middle Ordovician to mid-Cretaceous rocks are largely missing above the rift, partly due to nondeposition (Permian–Late Cretaceous) and partly due to late Paleozoic and/or mid-Cretaceous uplift and erosion, which produced a major unconformity at the top of the Paleozoic section.

The Mississippi Embayment contains up to 2 km of unconsolidated Upper Cretaceous to Upper Eocene marine and deltaic sediments locally overlain by Pliocene and Quaternary fluvial deposits of the Mississippi River (Autin et al., 1991). Direct sampling of the unconsolidated sediments was provided by the USGS New Madrid test well located near New Madrid, MO (Crone, 1981). Within the study area, unconsolidated sediment thickness reaches 800 m.

Two structural highs in Paleozoic rocks are associated with the majority of NMSZ seismicity. The CG-BA fault is coincident with the Blytheville arch, a 10 km wide zone of highly disrupted Paleozoic rocks trending along the axis of the Reelfoot Rift (Crone et. al, 1985; McKeown et. al, 1990). The Reelfoot fault is associated with the Pascola arch, an antiform produced during the late Paleozoic Ouachita/Appalachian orogeny (Marcher and Stearns, 1962).

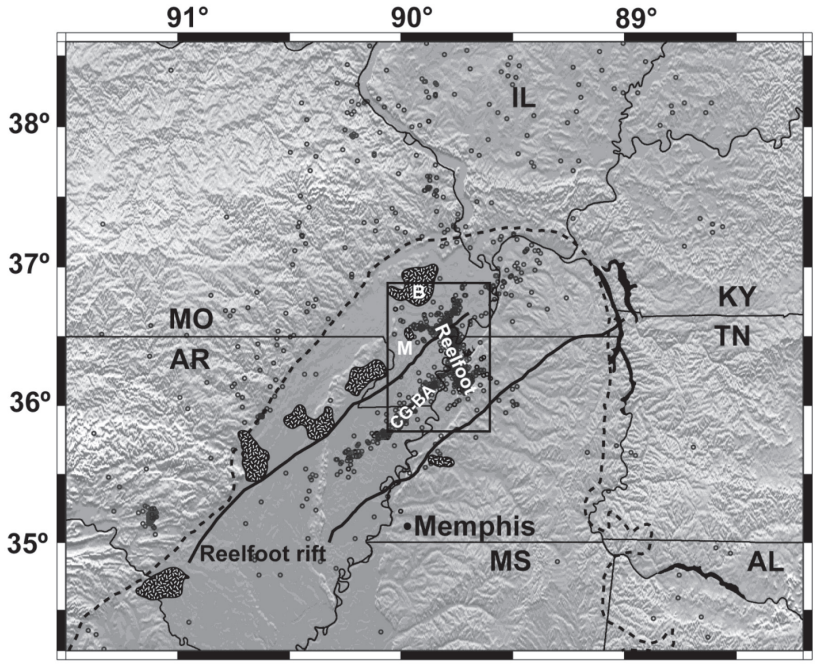

Figure 1. Topographic map for the central United States containing the New Madrid seismic zone. Earthquake epicenters from 1974 to present. The Reelfoot and Cotton Grove – Blytheville Arch (CG-BA) faults are indicated. Stippled areas indicate inferred plutons. Dashed lines indicate the Mississippi embayment and heavy solid lines trending NE-SW indicate the narrower Reelfoot rift. The box indicates the study region for the velocity inversion. Missouri (MO), Arkansas (AR), Tennessee (TN), Kentucky (KY), Alabama (AL), Illinois (IL), Mississippi (MS).

1. TomoDD Inversion for Vp, Vs and Hypocenter Locations

Background

In this study, we combine the PANDA arrival time dataset with additional P and S arrivals for local earthquakes recorded by the Cooperative New Madrid Seismic Network (CNMSN) to compute updated tomographic inversions for P and S velocity models and hypocenter locations. 3-D P and S wave velocity models are calculated using the program tomoDD (Zhang and Thurber, 2003). TomoDD utilizes the double difference algorithm used in the earthquake relocation program hypoDD (Waldhauser and Ellsworth, 2000; Waldhauser, 2001). TomoDD improves upon other local earthquake tomography programs by using catalog and waveform cross correlation (WCC) differential times in addition to catalog travel times, to solve for updated P and S wave velocity models and earthquake locations. Model resolution is examined through the use of synthetic tests. The improved tomographic images provide new insights into the velocity heterogeneity associated with NMSZ seismicity.

Method

TomoDD is a local earthquake tomography program that solves for 3-D P and S wave velocity structure as well as earthquake hypocenters using the double difference algorithm (Zhang and Thurber, 2003; Waldhauser and Ellsworth, 2000; Waldhauser, 2001). Catalog travel times and differential times are inverted simultaneously to solve for 3-D P and/or S wave velocity models and hypocenter locations. After each simultaneous inversion step for velocity and hypocenters, hypocenter locations are updated using the resulting 3-D model.

TomoDD is an improvement over other local earthquake tomography techniques in that it utilizes differential times in addition to absolute travel times. The differential times consist of catalog differential times (CT) as well as WCC differential times; these data provide further constraint on the earthquake relocations while minimizing error in the calculated velocity model associated with P and S wave catalog onset picks (Zhang and Thurber, 2003).

WCC can improve earthquake relocations and velocity models by providing more accurate P and S wave onset picks and hence initial travel times or by providing higher accuracy differential times directly (e.g. Dodge et al. (1995); Waldhauser and Ellsworth (2000)). The method of WCC used in this study compares waveforms of two phases at one station in the time domain (Horton et al., 2005). The waveforms are contained within a 1.28 second window. A bandpass filter is applied from 0.6 to 30 Hz to waveforms prior to cross correlation. The peak of the cross correlation function corresponds to a lag time that is equivalent to the differential time for that phase and the given event pair. A minimum correlation coefficient threshold of 0.7 is required for inclusion of the associated differential time into the dataset.

The 1-D velocity model established for the NMSZ is complicated, containing low velocity sediments at the surface and low velocities at 3 km depth (Table 1.1). The initial P wave velocity model is taken from Chiu et al. (1997). The S wave model used is a modification of the Chiu et al. (1997) model suggested by Pujol et al. (1997). The unconsolidated sediment unit at the surface transitions to relatively high velocities of 6.02 km/s associated with a known, 2 km thick limestone unit at approximately 1 km depth (Chiu et al., 1992). Several studies suggest that the limestone is underlain by a low velocity shale unit anywhere from 2-3 km thick (Catchings, 1999; Chiu et al., 1992). Velocity increases with depth starting at 5 km depth along a smooth gradient. The 1-D VELEST inversion program (Kissling et al., 1994) is used to test the validity of the input model using more recent CNMSN data. This procedure is done for P and S wave times individually, and we test a broad range of starting models. Most starting models converge to models featuring a low velocity zone at the expected depth range, and we therefore feel confident that the Chiu et al. (1992) model, as modified by Pujol et al. (1997) provides a good 1-D starting model for the 3-D inversion.

Due to the complex starting model and regional scale of the tomography problem, we use a version of tomoDD designed for regional problems that utilizes a finite difference ray-

tracer (Zhang, 2003). Finite difference ray-tracers are better able to model raypaths in the presence of sharp changes in velocity gradient, such as the NMSZ 1-D input model, and are more accurate at regional scales than the psuedo-bending ray tracing methods used within tomoDD for local scale studies. The velocity model is represented by a grid of nodes in three dimensions (Figure 1.1) and velocity between nodes is calculated via trilinear interpolation. This type of input allows for irregular grid spacing and yields a smooth gradient velocity model. Nodes are spaced closer within areas of high raypath coverage and systematically farther apart as resolution decreases. Raypaths and travel times are calculated within this velocity model using the finite difference ray tracing algorithm of Podvin and Lecomte (1991). In order to minimize computation time, the spatial boundaries of the finite difference grid can be defined independently (Zhang, 2003). For this study, the finite difference blocks are defined to be 700 meters in the x, y, and z directions. For this study, the horizontal node spacing within the densest region of seismicity is 5 km. The horizontal grid outside of the RF source region increases to a 10 and then 20 km node spacing. Vertical node spacing reflects a priori information from previous studies in this region. The top two nodes are at or near the surface (0 km and 1 km depth) to account for the thick sediment cover. The following node at 3 km depth is the top of the low velocity zone. The fourth node is at 5 km depth and represents the base of the low velocity zone. All other nodes are spaced 3 km apart.

TomoDD employs a hierarchical weighting scheme. P and S absolute travel times as well as catalog and cross correlation differential times can be weighted independently for each iteration. The absolute travel time data are weighted higher during initial iterations to establish coarse results. Gradually, the absolute data are down weighted in favor of the CT data and then the CT data are down weighted to allow additional refinement using the WCC data. The final weighting scheme for the absolute and differential times used in this study in shown in Table 1.2. Smoothing and damping are applied during inversion to stabilize the solution (Zhang and Thurber, 2003). Smoothing and damping values are determined for our study by running several single iteration inversions and comparing trade off curves between model variance and data variance. Smoothing values between 10-20 are determined to be reasonable. Selection of the final smoothing and damping values of 20 and 100, respectively, is determined using synthetic checkerboard modeling. Residual weighting is used to down weight or reject data with large residuals. The residual weighting used in this study ranges from 4-8 throughout the iterations; this is a multiplication factor used in conjunction with the standard deviation within a bi-weight function that down weights or disregards observations with high residuals (Waldhauser and Ellsworth, 2000; Zhang and Thurber, 2003).

The data set consists of P and S wave arrivals recorded by the CNMSN between 2000 and 2007 and the PANDA array between 1989 and 1992. All arrivals are recorded on three component stations, and S wave arrival times are picked on horizontal components. The PANDA portion of the data set consists of 435 earthquakes recorded by 40 stations. The PANDA data includes 4522 P wave arrivals and 3953 S wave arrivals. This results in 18662 P wave differential times and 16354 S wave differential times. The CNMSN dataset contains 837 earthquakes recorded between 2000 and 2007 at 135 stations. A total of 15146 P wave and 10387 S wave travel times are used, yielding 63321 P wave

differential times and 37187 S wave differential times. In addition, 37040 P wave and 18731 S wave WCC differential times are included. Combined, a total of 19668 P wave onsets and 119023 P wave differential times are included, as well as 14340 S wave onsets and 72272 S wave differential times. The final dataset represents a subset of the initial CNMSN and PANDA catalogs. Only events with 8 or more P wave arrivals were included. Additionally, events are declustered because hypocenters are unevenly distributed across the volume and concentrated along the RF. Declustering removes overly redundant raypaths by only including events that have the most observations in relation to other events within 0.5 km (Thurber et al., 2007). The removal of overly redundant raypaths allows for smoother results throughout the entire model volume. Events located outside of the model boundaries are also removed.

Resolution

Resolution is explored using three methods: 1) Computation of derivative weight sum (DWS) values, 2) synthetic restoring tests, and 3) synthetic checkerboard models. The DWS provides information on areas with the densest raypath coverage. The restoring tests are used to constrain how specific velocity anomalies would be recovered using the given data coverage. Checkerboard synthetic tests are used to determine how well velocity amplitude is recovered under a range of grid node spacing, smoothing, damping, and weighting parameters. Also for all synthetic tests, random noise of plus or minus 0.02 seconds and 0.04 seconds is added to the theoretical P wave and S wave travel times, respectively. This noisy data is then used to construct synthetic differential time measurements. The synthetic tests are designed to test the same source and station geometry as the final NMSZ data set.

Derivative weight sum

An initial measure of resolution is determined by examining the DWS, which is a measure of weighted raypath coverage (Thurber, 1983). Areas with a high DWS value are considered to be those with the best resolution. The regions along the areas of seismicity have the highest DWS, especially the RF. Areas with DWS values less than 50 are held fixed during the inversion to provide further stability to the solution. The best resolution is obtained in those areas with a DWS value of 250 or greater, based on synthetic tests.

Synthetic tests

We perform the restoring test by calculating synthetic arrival and differential times for P and S waves through an idealized model. The test placed low velocity anomalies in the region associated with RF seismicity at 5, 8 and 11 km depths. A region of high velocities is placed in the center of the RF at 5 and 8 km to test resolution in the case of overwhelmingly low velocities. Two high velocity anomalies are included at 5, 8 and 11 km depth in a region where previous results have imaged a mafic intrusion (Vlahovic et al., 2000). Finally, a high velocity anomaly is located at the northern model boundary to test potential artifacts in this region. The inclusion of a possible intrusion tests resolution and smearing outside of the RF source region as well as vertical smearing into the low velocity zone (3km depth).

The P wave model has 80-100% recovery of anomalies over a depth range of 5-8 km along the RF. The small area of high velocities in the central portion of the RF is distinguishable, also with 80-100% anomaly recovery at 5 and 8 km. The general low velocity trend is seen at 11 km depth but amplitude recovery is poor. There is recovery on the order of 50-90% of both anomalies associated with the mafic intrusion at 5 km. However, they are smeared together. Recovery associated with the larger intrusion anomaly is about 50-85% at 8 km and 65-90% at 11 km but the size and shape of the anomaly is not completely recovered. There is some vertical smearing of low and high velocities on the order of plus or minus 1-4% change from the input 1-D model into the low velocity zones at 1 and 3 km depth. Horizontal smearing of the low velocities outside of the RF source region at all depths is also on the order of 1-4%. Thus, we take 4% to be the minimum anomaly that we will interpret in the real P wave velocity model.

Restoring test results for the S wave model indicate 60-95% amplitude recovery of low velocities near the RF at 5 and 8 km depth. The high velocity anomaly placed along the central RF is recovered at 30-80% from 5 and 8 km, suggesting that small-scale anomalies may be difficult to image in the S wave velocity model. There is limited recovery of the low velocity anomalies along the RF at 11 km. The larger of the two high velocity intrusions is imaged at 5, 8 and 11 km. There is a 50-75% recovery of high velocities at 5 km; however, the starting shape of the anomaly is not recovered. The shape of the anomaly is recovered at 8 km with a 40 to 65% recovery of the original input velocity perturbations. There is limited recovery of this feature at 11 km. The S wave synthetics exhibit smearing into the low velocity zones on the order of 1-6% from the 1-D input model for both low and high velocities. Additionally, there is horizontal smearing, mainly of low velocities, on the order of 1-4%. We take these values to approximate resolvable anomalies and smearing in the S wave velocity model results.

Absolute travel times and differential times are also calculated for synthetic checkerboard velocity models consisting of two layers with anomalous velocities of plus or minus 10% within the 1-D velocity model. All anomalies are calculated along a single node. Two synthetic checkerboard tests are performed. In run 1, anomalies are placed at depths of 3 and 8 km. All other depth nodes have no associated anomalies. Anomalies are placed at depths of 5 and 11 km for run 2. P wave velocity synthetic results indicate highest resolution at depths of 5 and 8 km, similar to the restoring tests. Anomaly recovery is highest along the RF, with amplitude recovery on the order of 80-100%. Along the CGF-BA and north of the RF, most anomalies are recovered, but with only 70-80% of the input magnitude. The top of the low velocity zone corresponds to a depth of 3 km. The P wave velocity synthetic model results for 3 km from run 1 show some recovery of high velocity anomalies, on the order of 50-60% of the input magnitude. However, recovery of low velocity anomalies is poorer. Some high velocity anomaly magnitudes, on the order of 40-60%, are recovered at 11 km in the P wave velocity synthetic model in the RF source region. Therefore, there is limited resolution of high P wave velocity perturbations at depths of 3 and 11 km and even less resolution of low velocity perturbations. Synthetic results for the P wave model for runs 1 and 2 show some vertical and horizontal smearing between nodes, on average approximately 1-3% relative to the 1-D input model. The surfaces at 0 and 1 km depths show no significant vertical smearing for P wave velocities.

Synthetics for the S wave velocity solution confirm that there is resolution within a smaller horizontal area than in the P wave velocity solution, as shown by the DWS values. Similar to the P wave synthetic model results, the areas of highest resolution for the S wave velocities are at depths of 5 and 8 km along the RF. Within regions directly associated with seismicity, the checkerboard pattern and magnitude recovery is 80-100% for high velocity anomalies and 60-70% for low velocity anomalies. Resolution decreases rapidly moving away from the RF with a magnitude recovery of 60% at 5 km depth and less at other depth nodes. There is some high velocity recovery on the order of 50-75% of the input velocity at 3 km depth. However, there is almost no recovery of input low velocity anomalies. Additionally, run 2 indicates vertical upward smearing of as much as 40% of anomalies placed at 5 km depth. At 11 km depth, some high S wave velocity anomalies are recovered near the RF, but no low velocity anomalies are recovered. The S wave smearing results are consistent with those seen in the restoring tests.

The effect of the sediments at the surface is always problematic (Powell and Withers, 2009). The unconsolidated low velocity sediments are difficult to model accurately and structures within the sediments can be mapped into deeper features as a result. Synthetic tests using the data set presented in this study indicate there is no resolution at the surface (0 km depth node). When a checkerboard anomaly pattern of +/-10% is placed at the surface, there is no recovery of the checkerboard pattern; only a 5% high velocity anomaly is present at the surface. An approximately 1-2% velocity perturbation is also present in area below the sediments (Z= 1km) for the P wave synthetic results. The S wave results show a similar high velocity perturbation at the surface and high velocity smearing of up to 7% down to 1 km depth and 4% at 3 km depth.

Results

Inversion of the real data produces an overall WCC RMS reduction of 14% and the catalog differential times RMS is reduced by 39%. Results for the P and S wave velocity models and Vp/Vs ratio are presented in Figures 1.2-1.5. Interpretation will focus on features with velocity perturbations relative to the starting1-D model of plus or minus 4% that lie within the 250 DWS contour. All figures, other than the Vp/Vs ratio, show the percentage change of the resulting velocity model relative to the 1-D input model.

P-wave velocity solution

Small velocity anomalies are found for the top two depth nodes at 0 km and 1 km depth. Synthetic models do not support interpretation of these features because they are less than 4%. The most prominent high velocity anomaly at the third node is 3 to 4% greater than the 1-D initial model and is located at the northern limit of the northwestern arm of seismicity (A in Figure 1.2). According to the synthetic tests, high velocities can be resolved within the low velocity zone (third node). Low velocity anomalies are not well constrained, and interpretation of any low velocity features over this depth range cannot be supported with synthetic modeling.

At 5 km depth, low velocity anomalies are present throughout the entire NMSZ source region (Figure 1.2). The northern section of the RF has low velocity anomalies only on

the order of 2% but the southern region has more significant low velocity perturbations, reaching -5% in the immediate area of seismic activity and -7% at the southern limit of seismicity (B in Figures 1.2 and 1.4). The low velocity anomalies continue to the southwest along the CGF-BA complex. The amplitude of low velocity anomalies is reduced at 8 km depth but is still on the order of 3-4%. There are also low P wave velocities associated with seismicity at 11 km depth although resolution is reduced at this depth. The entire resolvable crustal volume southeast of the CGF-BA complex is slow relative to crust located to the northwest.

S-wave velocity solution

S wave synthetics indicate low resolution at 0 and 1 kilometers depth, but there is one significant anomaly in this depth range; a 3-4% high velocity anomaly is present at the northern limit of the northwestern arm of seismicity. This same high velocity anomaly appears at 3 kilometers depth, also with a 3-4% perturbation (A in Figure 1.2). The amplitude and size of this anomaly is largest at 5 km, where it is 4-7%. The amplitude decreases to 3-4 percent at 8 km depth. Synthetic models show that perturbations in this area do not have 100 percent amplitude recovery. Therefore, these results reflect a minimum estimation of the magnitude of the anomaly. Along the northern segment of the RF, S wave velocity perturbations are high and on the order of 2%, but this is within our expected amplitude error. The southern section of the RF is associated with low velocity anomalies of 5-6 percent between 3-8 km depth, similar to the P wave solution (B in Figures 1.2 and 1.5).

Vp/Vs ratios

Vp/Vs ratios are calculated from the P and S wave velocity models via direct division of absolute velocities (Figure 1.3). Resolution is not identical for the P and S wave results and this may bias our Vp/Vs estimates (Eberhart-Phillips, 1990; Eberhart-Phillips and Reyners, 1997; Reyners et al., 1999). We consider the Vp/Vs ratio fairly accurate for areas of similar P and S wave resolution, primarily within the densest region of seismic activity, and within the DWS 250 contour for the S wave inversion results. The Vp/Vs ratio associated with the NMSZ arms of seismicity at 5 and 8 km depth is low relative to the 1-D starting model value of 1.73. This reflects the fact that P wave velocity values were reduced more than S wave velocity values in the joint inversion. Synthetic tests indicate S wave velocity recovery is not as high as P wave velocity recovery, suggesting that using a direct division approach may actually underestimate Vp/Vs ratios across the entire region. There is one significant anomaly, a high Vp/Vs ratio imaged in the central portion of the RF (C in Figure 1.3). The high ratio results from normal P wave velocities and reduced S wave velocities. While the absolute Vp/Vs value may not be accurate, the fact that this small region is high relative to the surrounding material is likely not an artifact.

Discussion

Velocity structure within the NMSZ is examined in several previous studies. Mooney et al. (1983) and Catchings (1999) conduct detailed seismic refraction surveys. Mooney et al. (1983) find an average crustal thickness of 41 kilometers and a crust composed of 6 layers. They suggest the existence of a 3 km thick low velocity zone from 3-6 km depth

composed of marine shale deposited after rifting. Catchings (1999) finds a low velocity upper crust (4 km thick) and a complex horst and graben system within the upper crustal Reelfoot rift. Earthquakes within the NMSZ appear to concentrate around or below one of these horst structures. Chiu et al. (1992) examine faulting in the NMSZ using the PANDA data. They find a low Vp/Vs ratio (1.51) layer located at depths of approximately 3 to 5 km and they conclude that this is due to low P and S wave velocities associated with the presence of shale. High-resolution 3-D P wave and S wave velocity models, as well as Vp/Vs ratios are determined for the NMSZ by Vlahovic et al. (2000) and Vlahovic and Powell (2001). Their P and S wave velocity models are calculated with the PANDA dataset using the inversion method described in Benz et al. (1996). Their P wave velocity model indicates a low velocity zone associated with seismicity at the southern end of the RF.

The most prominent high P and S wave velocity anomalies in the tomoDD solutions occur at the northwestern end of seismicity (A in Figure 1.2). This high velocity anomaly correlates spatially with known high gravity and magnetic anomalies (Hildenbrand and Hendricks, 1995; Rabak, 2009). The high velocity anomaly does not exactly coincide with the location of the gravity and magnetic highs but is located slightly to the northwest. The potential field anomalies are thought to be indicative of a mafic intrusion. The S wave velocity model indicates that the intrusion is present down to 8 km depth. However, P wave velocity results at this depth show only minor velocity perturbations within error bounds. Therefore, the presence of the high velocity anomaly can only be inferred to a depth of 5 km. In addition to gravity and magnetic evidence, the presence of this mafic intrusion has been imaged in the previous tomography results of Vlahovic et al. (2000). There appears to be a spatial relationship between seismicity and this high velocity anomaly; the seismicity along the northwestern segment of the NMSZ terminates upon encountering the intrusion. This suggests that the intrusion acts as a barrier to the propagation of earthquakes along this segment, as suggested by Vlahovic et al. (2000) and Vlahovic and Powell (2001).

The northern section of the RF acts as a left step-over between two right lateral strike slip faults, the CGF-BA complex and the northeastern arm of seismicity (Odum et al., 1999; Schweig and Ellis, 1994; Russ, 1982). P and S wave velocities along the northern RF are represented adequately by the 1-D starting model and only show small-scale variations. There is a magnetic anomaly in this region known as the Reelfoot Magnetic Anomaly (RMA), which is produced by an intrusive body (anomaly O in Hildenbrand and Hendricks, 1995; Rabak, 2009). The northern segment of the RF coincides with the RMA, and the presence of the intrusion could be playing a role in the increased seismic activity along this portion of the RF. However, there are no significant velocity anomalies resolved that correspond to the RMA.

The southern portion of RF seismicity does not represent a left step over fault as it lies south of the CGF-BA complex. The P wave velocity model indicates low velocities associated with earthquake occurrence along the southern portion of the RF. This association is established in previous studies (Vlahovic et al., 2000; Al-Shukri and Mitchell, 1988). Our results indicate the area of lowest velocities extends further south

along the RF than indicated in Vlahovic et al. (2000). The overall trend of low velocities in our study and in Vlahovic et al. (2000) is consistent and magnitudes of the anomalies are comparable; both studies indicate velocity perturbations on the order of 4-7%. Slight differences could be due to differences in resolution or smoothing parameters. The decrease in P wave velocities could coincide with a decrease in crustal strength, which results in the occurrence of microearthquakes (Zhao et al., 1996). The southern portion of the RF also shows a significant decrease in S wave velocities. Figures 1.2, 1.4 and 1.5 illustrate minimal velocity perturbations associated with seismicity along the northern RF and increasing low velocity anomaly magnitude moving south along the southern RF in both the P and S wave velocity models. Vlahovic et al. (2000) and Al-Shukri and Mitchell (1988) attribute the decreased velocities to increased pore pressures. Focal mechanisms along the southern portion of the RF suggest increased variability in slip motion in this area. Out of 87 solutions in this region, there are 40 exhibiting reverse, 34 strike slip, and 13 normal motion (Johnson, 2008). Additionally, there are two swarms associated with this area (labeled with a star on Figure 1.1). The first of these swarms occurred in 2001 and the second in 2008. The 2001 swarm contained 10 catalog events and the 2008 swarm contained 22. Both swarms occurred at 6-7 km depth (Bisrat et al., 2008). The variability in slip motion as well as the presence of earthquake swarms suggest the possibility of a highly fractured area with increased pore pressure, thus decreasing shear stress allowing more slip along these fractures (Miller et al., 1996).

An abundance of fractures and increased pore pressure would produce a decrease in both the P and S wave velocities, which is consistent with the tomography results (Nur and Simmons, 1969; Moos and Zoback, 1983; O'Connell and Budiansky, 1974). The area of decreased velocities is associated with the depths containing the majority of RF seismicity. However, the velocity models do not indicate a strong decrease in P or S wave velocities below 8 kilometers depth (Figures 1.2, 1.4, and 1.5). The change in velocity perturbation could be associated with a decrease in the density of seismicity below 8 km depth (Figures 1.2, 1.4 and 1.5). The decrease in velocities could also be a result of decreased resolution in the P and S wave velocity models, since raypath coverage is diminished below 8 km.

Previously, decreases in P and S wave velocities have been associated with earthquake source regions. Seismicity recorded after the Kobe, Japan 1995 main shock occurred in regions with lowered P and S wave velocities. The decreases in velocities are attributed to increased fracturing and fluids in the source region (Zhao et al., 1996). Seismicity in the NMSZ occurs primarily in the crystalline basement, and the effect of increased fractures and pore pressures in crystalline rock is shown to decrease P and S wave velocities (Nur and Simmons, 1969; Moos and Zoback, 1983; O'Connell and Budiansky, 1974). Additionally, variability in fracture density is also shown to lead to variability in velocities, with more intense low velocities being associated with higher density of fracturing (Moos and Zoback, 1983). The low Vp/Vs ratios within the NMSZ at 5 and 8 km depth are consistent with ongoing tomography work using other local earthquake tomography methods in this area (see below). The low ratios coincide with NMSZ seismicity and could be indicative of property changes over the entire seismic zone that are difficult to image due to resolution constraints. One area of interest highlighted by the

Vp/Vs ratio results of this study is that a high ratio anomaly occurs just to the west of the central segment of the RF (C in Figure 1.3). A high Vp/Vs ratio produced by normal P wave velocities and low S wave velocities, as occurs here, could be indicative of the shape of cracks in this region. The presence of cracks reduces the elastic moduli of the rock and reduces both P and S wave velocities. The presence of flat cracks (low aspect ratio cracks) has more effect on the S wave velocity due to the particle motion of S waves (Wilkens et al., 1984). We note that the high Vp/Vs ratio occurs near the intersection of the CGF-BA complex and the RF and also near the region in which the RF changes dip and strike. Ongoing research is focusing on high-resolution Vp/Vs ratios of the NMSZ using direct inversion of S-P data.

Conclusions

Three-dimensional P and S wave velocity models are constructed for the NMSZ using the double difference tomography method of Zhang and Thurber (2003). P and S wave velocity solutions indicate a high velocity anomaly at the northwestern extent of seismicity along the northwestern arm of the seismic zone (A in Figure 1.2). The region is associated with a mafic intrusion that has both high gravity and magnetic signatures (Rabak, 2009; Hildenbrand and Hendricks, 1995).

The RF naturally divides into two regions based on the velocity modeling results and previous investigations using only microseismicity (i.e. Pujol et al. (1997), this study). Results indicate low P wave velocity anomalies along the southern RF, consistent with previous findings (Vlahovic et al., 2000; Al-Shukri and Mitchell, 1988). The northern portion of the RF has minimal velocity perturbations and is not significantly different from the 1-D starting model, whereas the southern portion of the fault has anomalies as low as 7 percent. The S wave model velocity is similar to the P wave velocity model. The northern region of RF seismicity is close to the 1-D starting model. The southern portion has significant negative velocity perturbations.

The Reelfoot Magnetic Anomaly (RMA) is also associated with the northern portion of RF seismicity. However, our tomography results indicate no significant change in P or S wave velocities from the 1-D starting model. The southern portion of the RF could be associated with increased fracturing and pore pressures, coinciding with the imaged decrease in P and S wave velocities (B in Figures 1.2, 1.4, and 1.5). The decrease in seismic velocities associated with the southern RF suggests a significant change in the properties of the rocks in this portion of the fault. Vp/Vs ratios are also calculated for the area. Low Vp/Vs ratios associated with the NMSZ arms of seismicity are found and are the focus of ongoing research. The most interesting feature found in this study is a Vp/Vs high produced by normal P wave velocity and low S wave velocity perturbations (labeled C in Figure 1.3). This region is associated with a change in strike of the fault itself. This area is also interpreted to be associated with an increase in fracturing and pore fluid pressures and possibly an increase in the amount of flat (low aspect ratio) cracks present.

Table 1.1. Starting 1D P- and S-wave velocity models

Depth	P-wave	S-wave	Description

(km)	Velocity (km/s)	Velocity (km/s)	
0.00 – 0.65	1.8	0.6	Unconsolidated Upper Cretaceous to recent sediments
0.65 – 2.65	6.02	3.48	Paleozoic surface: Late Cambrian – Early Ordovician Knox dolomite and limestone
2.65 – 4.65	4.83	2.79	Early – Middle Cambrian Elvins shale
4.65 – 17.0	6.17	3.56	Precambrian crystalline upper crust
17.0 - Moho	6.6	3.8	Precambrian crystalline lower crust

Table 1.2

Iterations	Absolute Data P	Absolute Data S	Catalog DT P	Catalog DT S	CC DT P	CC DT S
1-6	1.0	0.8	0.1	0.08	0.1	0.08
7-9	0.1	0.08	1.0	0.8	0.1	0.08
10-12	0.1	0.08	1.0	0.8	1.0	0.8
13-15	0.1	0.08	0.1	0.08	1.0	0.8

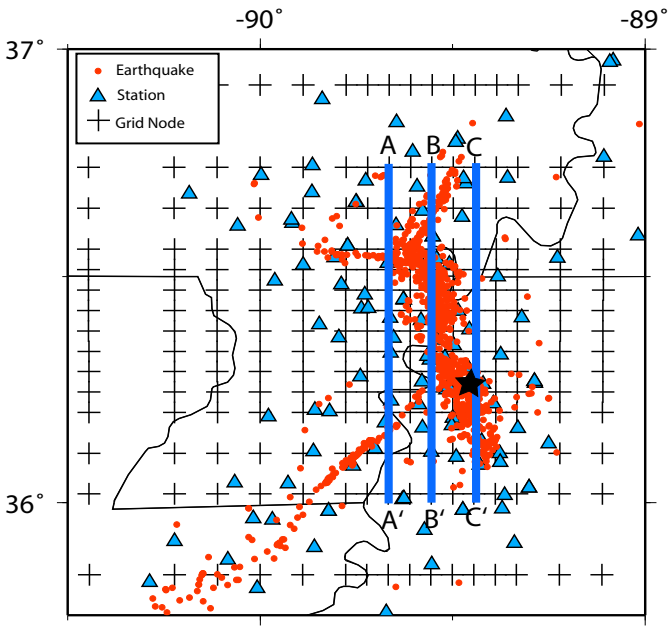

Figure 1.1. Station coverage and grid node spacing used in the inversion. Triangles are stations, crosses are nodes, circles are earthquakes. Vertical blue lines indicate cross sections corresponding to Figures 2.15 and 2.16.

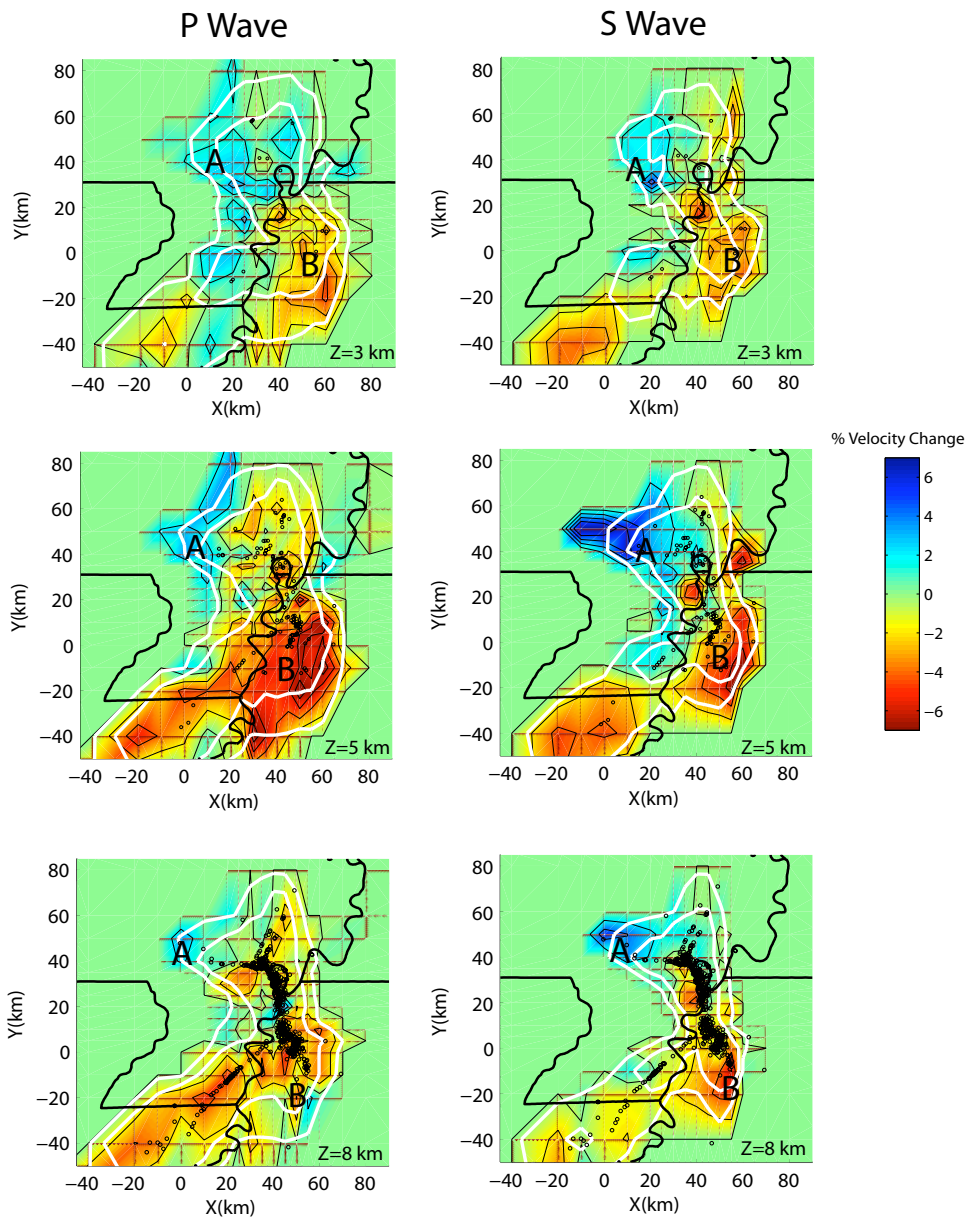

Figure 1.2 Final P and S wave velocity models at 3, 8, and 11km. P wave velocity results are shown on the left and S wave velocity results are on the right. White contours indicate areas with a DWS value greater than 50 (outer) and 250 (inner). Black contours indicate 0, 2, 4, and 6 percent velocity perturbations. Circles represent seismicity occurring vertically within 1-1.5 km of each depth node. 'A' indicates a significant high velocity perturbation and 'B' refers to an area of significant low velocity perturbations discussed in the text.

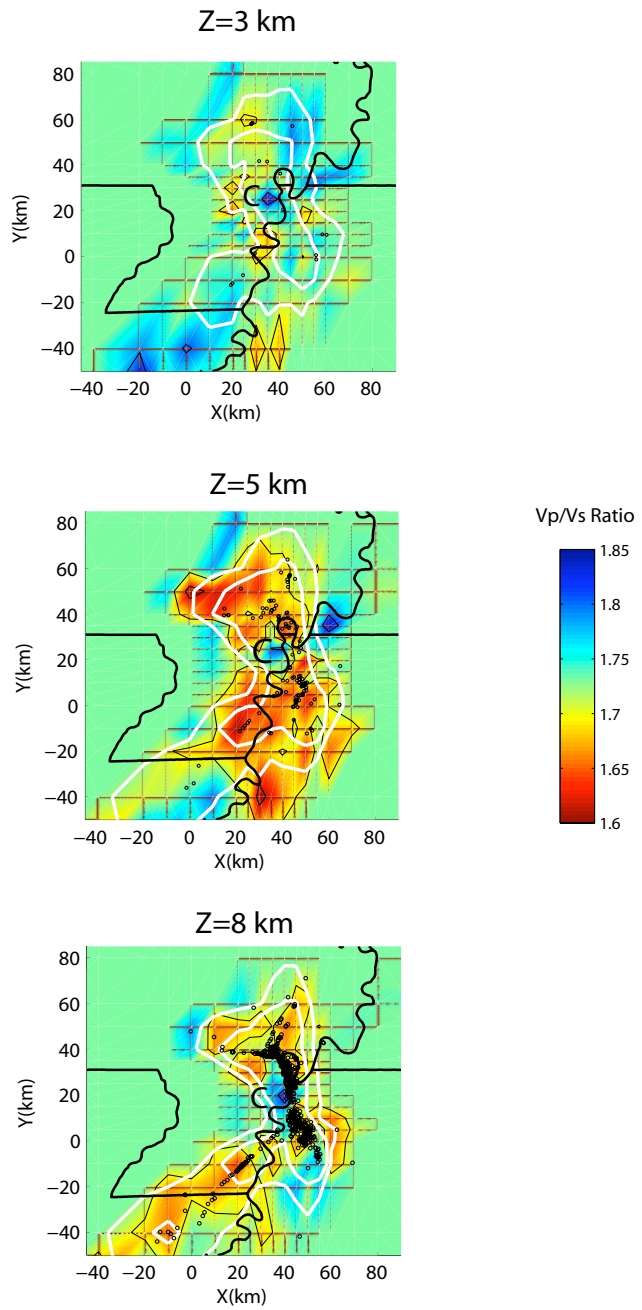

Figure 1.3 Final Vp/Vs models at 3, 8, and 11km. Black contours are placed at Vp/Vs ratios of 1.6, 1.7, and 1.8. The white contours indicate areas with comparable DWS values of 50 (outer) and 250 (inner) taken from the S wave velocity model. Circles represent seismicity occurring vertically within 1-1.5km of each depth node.

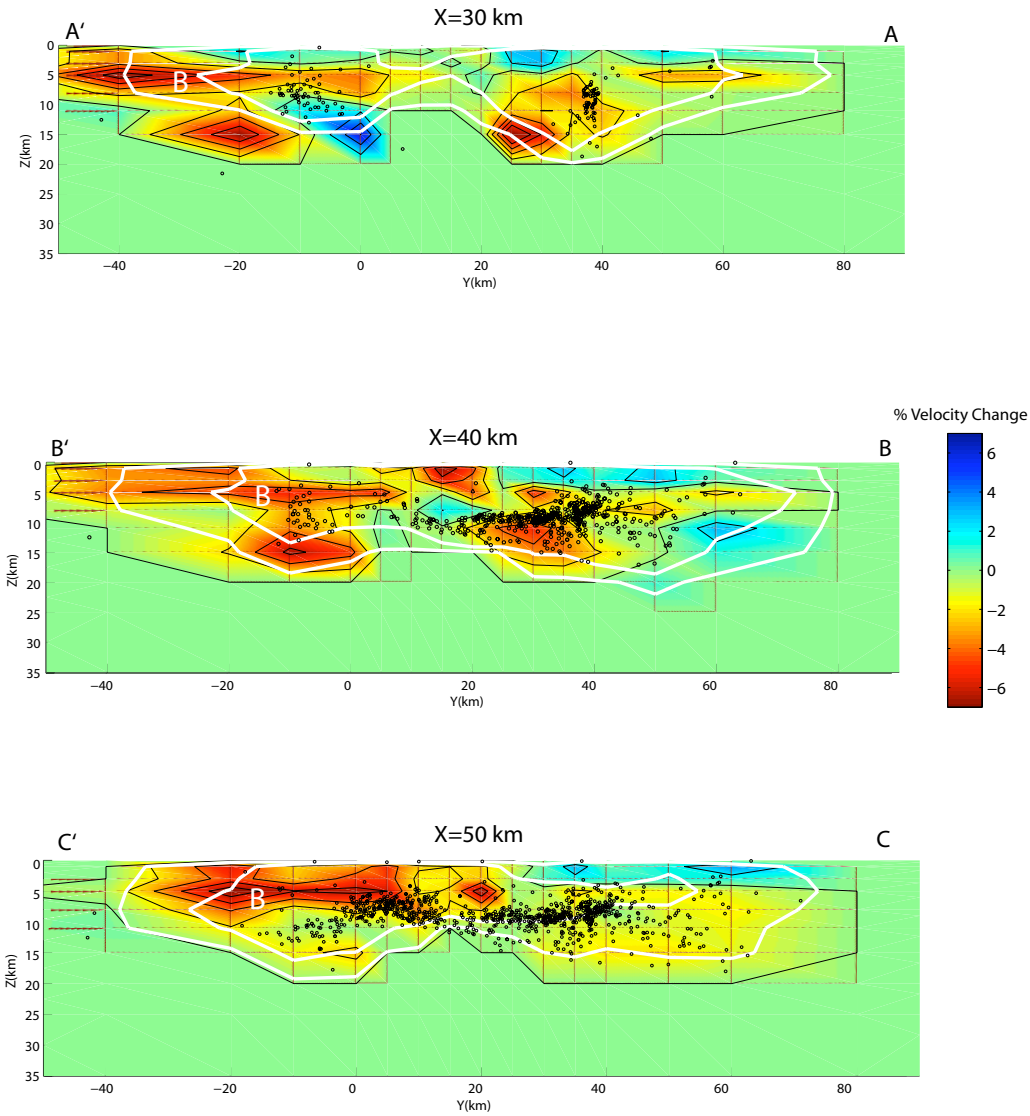

Figure 1.4 P wave velocity model shown in cross sections (see Figure 2.1 for locations). Cross sections run north-south along lines of longitude. Cross section A-A' is at X=30 km and shows seismicity along the CGF-BA and the northwest arm. Cross section B-B' is at X=40km and C-C' is at X=50km; both pass through the RF. Two white contours indicate DWS values of 50(outer) and 250(inner). Black circles are seismicity. Black contours indicate velocity perturbations of 0, 2, 4, and 6 percent.

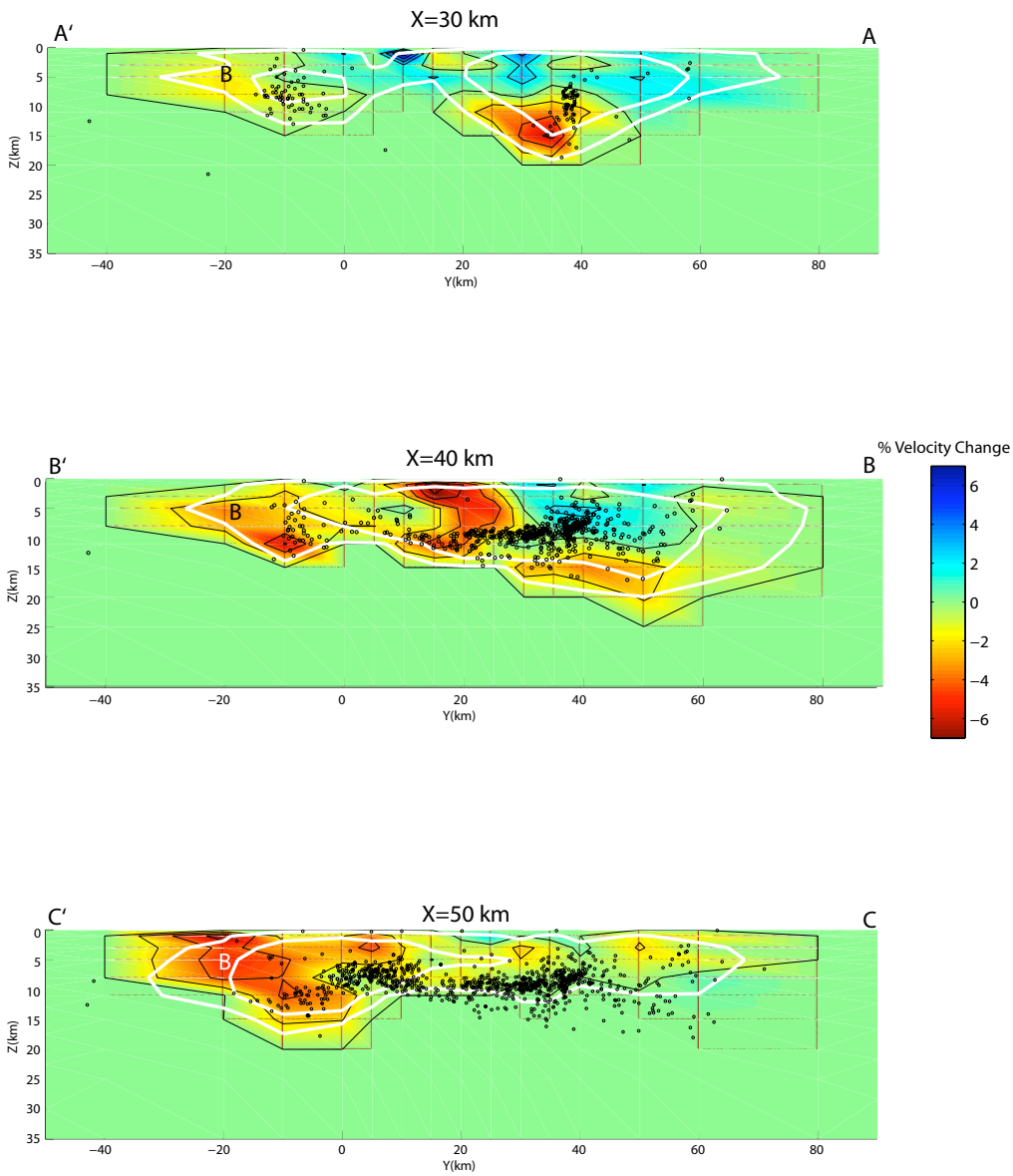

Figure 1.5 S wave velocity model shown in cross sections (see Figure 2.1 for locations). Cross sections run north-south along lines of longitude. Cross section A-A' is at X=30 km and shows seismicity along the CGF-BA and the northwest arm. Cross section B-B' is at X=40km and C-C' is at X=50km; both pass through the RF. Two white contours indicate DWS values of 50(outer) and 250(inner). Black circles are seismicity. Black contours indicate velocity perturbations of 0, 2, 4, and 6 percent.

2. The Effects of Mississippi Embayment Sediments on Local Earthquake Tomography

Background

Velocity perturbations associated with the NMSZ are investigated using a local earthquake tomography (LET) code developed by Benz et al. (1996) and modified by Tryggvason et al. (2002) to invert for both P and S wave velocity structure. As a first step in this inversion procedure, we investigate the effects of velocity and thickness variations in the thick, unconsolidated Mississippi Embayment sediments on the tomography results. This is a necessary step before the tomography solutions can be interpreted in terms of deeper structure. The presence of the low velocity sediments is particularly problematic because they cover high velocity Paleozoic carbonate rocks, resulting in a large velocity contrast. Conceivably, lateral variations in sediment thickness could introduce significant travel time variations (Pujol, 2006). In previous LET inversions for P- and S-wave velocity structure using NMSZ arrival time data recorded by the digital, three-component PANDA network (Chiu et al., 1992), station corrections were determined and removed to compensate for embayment sediment thickness and velocity variations (Vlahovic et al., 2000; Vlahovic and Powell, 2001). Each station correction should be influenced primarily by structure directly under the station because ray paths in the top layer of unconsolidated, low velocity sediments are almost vertical. However, the highly clustered distribution of hypocenters in the NMSZ could make the corrections sensitive to systematic velocity variations along deeper portions of the ray paths. Indeed, it was found that the primary effect of removing station corrections in both the P-wave and S-wave velocity inversions was to diminish the magnitudes of the velocity anomalies in the upper four km (Vlahovic and Powell, 2001). Station corrections alone do not provide enough information to determine the extent to which the three-dimensional structure of the sediments affects the inversion results. In this study, we investigate the influence of the low velocity sediments on LET using three-dimensional synthetic models and independent information on sediment thickness and velocity structure (Bodin et al., 2001).

Starting velocity model

The starting model used in this study is given in Table 1.1. The crust hosting the NMSZ can be divided in a vertical sense into five primary layers, as indicated in Table 1.1. A more detailed study of unconsolidated sediment thickness in the northern portion of the Mississippi embayment was conducted by Dart (1995) using drill hole data and USGS and COCORP vibroseis lines. Dart (1995) created a Paleozoic surface structure contour map (equivalent to the thickness of the unconsolidated sediments below sea level) using subsurface stratigraphic depths from 578 drill holes and core holes as well as 308 shot point locations along 31 vibroseis lines. This contour map captures first order variations in sediment thickness and is used in this study to remove the effects of the sediments from the tomographic images of P and S wave velocities.

Data and Tomographic Method

Arrival times used for the velocity inversions are taken from NMSZ network data recorded over the four-year period 2000 to 2005 and PANDA data recorded from 1989 through 1992. The combined data set, after requiring a minimum of four P- and S-wave arrivals per earthquake, consists of 12,566 P wave arrivals and 8,771 S-wave arrivals. There is some overlap of PANDA and network station coverage but the combined data set yields an average station spacing of roughly 8 km (Figure 2.1). The total number of stations is 97 and the total number of earthquakes used is 1,172. Approximate picking errors for P-waves and S-waves are 0.02 and 0.08 s, respectively. High precision of the arrival time picks is insured by using times with the best empirical weights.

We use a modified version of the nonlinear travel-time tomography method of Benz et al. [1996] to create 3-D P- and S-wave velocity models and determine hypocenter relocations. The modification allows P-and S-wave velocity models to be determined independently using the approach described by Tryggvason et al. (2002). The 80 km by 120 km by 24 km inversion volume is parameterized into cells with constant velocity. The size of the cells is 2 km by 2 km horizontally by 2 km in the vertical direction, and is based on the source-receiver distribution. Arrival times are calculated using the finite difference method of Podvin and Lecomte [1991] with a 160 by 240 by 48 node grid with uniform 0.5 km spacing between nodes. The nonlinear solution is obtained by iteration over linear inversions, so that ray paths are updated in the latest 3-D velocity model. We use constraining equations that minimize the roughness of the slowness field in order to stabilize the solution and minimize artifacts due to model parameterization [Lees and Crosson, 1989; Benz et al., 1996]. Smoothing parameters that control the trade-off between the minimization of arrival time residuals and roughness of the model are determined using a trial-and-error method and both synthetic and real data. Chosen smoothing parameters minimize artifacts in the solution while still resolving the magnitude of the synthetic anomalies. Cataloged earthquake locations are obtained using the 1-D, PANDA P-wave and S-wave velocity models determined by Chiu et al. [1992]. These 1-D models, shown in Table 1.1, are also used as the starting models in the velocity inversions.

Effects of the Unconsolidated Sediments

We investigate the effects of the unconsolidated sediments on the velocity inversions three ways. First, we test the assumption that station corrections record the effects of lateral velocity changes in the near surface and variable sediment thickness. Second, the effects of sediment structure are explored using synthetic models. Third, the effects of the sediments ("sediment correction") are removed using independent information regarding sediment thickness and velocity structure.

Station corrections are defined as the average station residuals after relocation of hypocenters in the starting velocity model. In general, the P wave corrections are less than ±0.1s. The exceptions are larger (up to 0.2s) average residuals associated with three stations located NW of the Reelfoot fault. These stations are part of the PANDA deployment. Two were located within a few kilometers of presently operating network stations but the network stations have smaller, positive average residuals. The observed discrepancy in residuals between the PANDA and network stations could be attributed to

different installation practices and equipment, or to different siting conditions. For example, network stations are installed in vaults while PANDA stations were not and the PANDA stations in question were located on levees to facilitate a now-abandoned telemetry requirement. The PANDA stations were retained in the study because there is no clear evidence that the data they generated is suspect. Moreover, removal of these stations did not produce detectable changes in the LET velocity solutions. Many S-wave residuals are larger than the associated P-wave residuals and most are negative. This suggests that the S-wave is being picked too early or that the S-wave velocity for the unconsolidated sediments in the starting velocity model is too slow. Problems with the velocity model are more likely, as the residuals tend to become more negative to the north, in agreement with thinning of the sediment package.

Several synthetic models are generated to test the effects of lateral velocity variations in the unconsolidated sediment layer on the velocity solutions. In all of these tests, we invert a synthetic data set constructed for the source-receiver geometry shown in Figure 2.1 and we use the same smoothing parameters and starting model used in the inversion of the real data. Synthetic models consist of chessboards of alternating positive and negative velocity anomalies or smaller regions of either positive or negative anomalies placed within the sedimentary layer. In some cases, anomalous regions are included deeper within the model to test the effects of velocity variations in the sediments upon the resolution of deeper structures. Modeled velocity anomalies within the sediments range between ± 4 and 12% relative to the starting model. Synthetic times are calculated using an analytical, 3D ray-tracing algorithm (Gupta and Roecker, 1993) to provide a data set that is not dependent upon the finite difference method of determining travel times used in the Benz inversion method. In addition, Gaussian noise of up to 10% is added to the computed travel times. Differences between synthetic travel times computed using the analytical method and the finite difference method are less than 0.05 s for both P and S waves and result in velocity models with comparable resolutions.

The effect of variable sediment thickness is investigated using the contour map developed by Bodin et al. (2002) based upon information contained in Dart (1995), additional estimates of Paleozoic surface depths provided by VanArsdale and TenBrink (2000), and surface topography. Sediment thickness beneath each station is determined from the contour map and travel times for P and S waves through the sediments are determined using the S-wave velocity versus depth relationship derived in Bodin et al. (2002) and a Vp/Vs ratio of 3.0. An assumption of vertical ray paths through the sediments is made; this will introduce travel time errors on the order of 0.01s, given that most earthquakes occur at depths greater than 5 km and the velocity contrast across the Paleozoic surface is very high. The Bodin et al. (2002) S-wave velocity versus sediment thickness relationship,

$$Vs = 521.15 + 0.37459H \qquad (1)$$

where H is thickness in meters, is appropriate over the depth range $350<H<1000$ meters. At shallower depths, the S-wave velocity decreases more rapidly than the relationship predicts (Bodin et al., 2002). We modified the relationship to allow S-wave velocities at

the surface to reach values of 125m/s, in accord with geotechnical observations (e.g. Romero and Rix, 2001). Our modified relationship is

$$Vs=125.0 + 1.50645H \text{ for } H< 350m. \quad (2)$$

The velocity inversion is adjusted to account for the removal of the sediments by assuming a new baseline of 860 m. New "station elevations" are defined as the difference between the sediment thickness beneath each station and the new baseline. Hypocenters and the velocity model are adjusted to the new baseline and twelve earthquakes, located above the new baseline, are eliminated. After the inversion is completed, hypocenters and layer depths are corrected to their positions relative to sea level.

Results

Synthetic modeling designed to test the effects of lateral velocity variations in the unconsolidated sediments produced consistent results. Velocity anomalies are not resolved in the sedimentary layer in either the P- or S-wave velocity solutions but are smeared into deeper portions of the inversion volume. For the P-wave velocity solutions, smearing extends into the layer just below the sediments but no deeper. S-wave velocity models are affected to greater depths, particularly by smearing of high velocity anomalies placed in the sedimentary layer. We examine a severe test involving a chessboard of alternating 10% positive and negative velocity anomalies placed in the sedimentary layer. Each anomalous region has horizontal dimensions of 8 by 8 km and is separated from its neighbor by a 4 km wide region of normal velocity. For the P-wave velocity model, a weak chessboard pattern can be observed in the layer just below the sediments but deeper layers are not affected. In the S-wave velocity model, the high velocity portions of the chessboard are smeared to depths of 6 km. Below this depth, anomalies are still present but do not exceed 1%. When velocity anomalies equal to or less than 4% in absolute magnitude are placed in the unconsolidated sedimentary layer, smearing from this layer does not produce velocity anomalies exceeding 1% in layers deeper than 2.65 km.

The effect of removing "normal" station corrections is a reduction in the magnitude of the velocity anomalies at all depths within the inversion volume. Otherwise, the solutions are very similar, down to the smallest resolved anomalies. In the case of the S wave velocity solutions, the primary effect of the station corrections is to also reduce the amplitudes of the velocity anomalies at all depths. Removing station corrections from the synthetic times generated for velocity anomalies placed in the unconsolidated sediment layer reduces the effects of smearing by roughly half; smearing is still apparent, particularly in the S-wave velocity models, but the magnitude of the anomalies due to smearing is reduced by about 50%.

The solutions obtained using independent information about sediment thicknesses and velocities (sediment correction removed from the real data) are very similar to the uncorrected solutions. Solutions obtained using the Bodin et al. (2002) S-wave velocity versus sediment thickness relationship (equation 1) are indistinguishable from those obtained using the modification indicated in equation 2. There is a reduction in anomaly

magnitudes over portions of the corrected velocity solutions, most notably in the northern portion (north of 36.5 °N) of the inversion volume. Here, the magnitudes of the low velocity anomalies are reduced in the P wave velocity solution while high velocity anomalies are reduced in the S wave velocity solution. With the exception of the northwest portion of the S wave inversion volume, the reduction in anomaly magnitude is less than that obtained using normal station corrections.

Discussion

The results of this study suggest that the presence of thick, unconsolidated sediments above the NMSZ has little effect upon crustal velocity models determined using local earthquake tomography. Velocity models obtained with unmodified arrival time data and those obtained after applying routine station corrections are very similar. As was found in previous studies involving the PANDA stations (Vlahovic and Powell, 2001), applying routine station corrections reduces the magnitude of the velocity anomalies in the inversion volume without altering the anomaly pattern. Applying station corrections does not simply remove the effects of velocity anomalies associated with structure located beneath individual stations. Rather, the highly clustered distribution of hypocenters makes the corrections sensitive to velocity variations along deeper portions of the ray path and removing station corrections actually removes desirable information from the velocity solutions. The effects of the unconsolidated sediments on the velocity solutions cannot be determined from this type of analysis alone.

Synthetic modeling provides further insight into the effects of the unconsolidated sediments on deeper structure. Strong lateral velocity variations in the sediments, if they exist, can influence P-wave velocity models for the uppermost portion of the Paleozoic sediments but have little effect on deeper portions of the inversion volume. As might be anticipated, smearing effects in the S-wave velocity models are more prominent and affect deeper portions of the velocity model. The velocity of S waves in the unconsolidated sediments is very low and the time spent in these sediments is proportionally high. Thus, lateral velocity variations and/or variations in the unconsolidated sediment thickness will have a much stronger influence on S wave travel times than on P-wave times. Smearing from velocity perturbations in the unconsolidated sediments produces anomalies with diminishing magnitudes as a function of increasing depth within the model.

Results from the synthetic models can be used to examine the role of smearing from the unconsolidated sediment layer on the velocity inversions obtained using real arrival times. The unmodified P and S-wave velocity solutions contain both high and low velocity anomalies that are very consistent from layer to layer and extend vertically throughout the inversion volume. In some instances, the magnitudes of the anomalies increase with increasing depth. Clearly, these observations are incompatible with smearing from the unconsolidated sediment layer. If the observed anomalies were produced by smearing effects, we would expect them to be much more prominent in the S-wave solution than the P-wave solution, extend to deeper portions of the S-wave solution, and diminish in magnitude as a function of depth. Thus the unmodified velocity solutions indicate that perturbations associated with the unconsolidated sediments do not

have a first order effect on the inversion results. Second order effects remain a possibility, particularly some smearing of high velocity anomalies associated with the unconsolidated sediments into the upper portion of the S wave velocity solution.

Removing the effects of the unconsolidated sediments using independent information about sediment thickness and velocity structure (the "sediment correction") proved to be sensitive to the velocities assigned to the sediments. Assigning constant P and S wave velocities results in unrealistic velocity solutions in the sense that changes in the velocity anomaly magnitudes produce unrealistic Vp/Vs ratios within deeper portions of the inversion volume. For example, using the sediment velocities indicated in the Table 2.1produce Vp/Vs ratios of less than 1.58 below the sedimentary layer across all but the northwest portion of the inversion volume. The solution obtained using the sediment thickness map and simple velocity versus thickness relationship determined by Bodin et al. (2002), yields reasonable Vp/Vs ratios in the range 1.81 to 1.66 within the inversion volume. The information provided in Bodin et al. (2002) is presently our best estimate for the unconsolidated sediment thickness and velocity structure across the embayment.

Interpretation of the P and S wave velocity models obtained by making the sediment correction is aided by examining all three solutions. As is the case when the normal station corrections are removed, applying the sediment correction reduces the anomaly magnitudes. The reduction is not as severe in the P wave solution but is comparable in the S wave solution. Thus, there is a suggestion that applying the sediment correction removes desirable information. There is no evidence that the sediment correction is removing smearing effects produced by velocity perturbations in the unconsolidated sediments. Note that the reduction in velocity anomaly magnitudes observed in the corrected S wave velocity solution applies primarily to high velocity features in the northern portion of the inversion volume. These features correspond to high velocity anomalies in the P wave velocity solution and extend vertically throughout the inversion volume; they cannot be attributed to smearing from surface features.

Although application of the sediment correction appears to be removing information from the inversion solution, the effect is not as pronounced as the loss of information observed when normal station corrections are applied to the P wave solution. In this sense, the sediment correction is an improvement over normal station corrections. In fact, the agreement between the unmodified velocity solution and the P and S wave velocity solutions obtained after the sediment correction is remarkable, given the crude specification of unconsolidated sediment velocity and thickness used to make the correction. The greatest discrepancies between the corrected and unmodified solutions occur north of about 36.5°N. This is one of the least constrained portions of the sediment thickness map produced by Dart (1995). Our results suggest that more detailed maps of sediment thickness and more detailed specification of velocity variations could be used to remove second order effects of the unconsolidated sediments on LET solutions. The unconsolidated sediments do not appear to be exerting a first order effect on the velocity models.

Conclusions

The primary objective of this study is to determine the effects the unconsolidated embayment sediments on LET results. Removing normal station corrections diminishes velocity anomaly magnitudes in the inversion solution and does not change the anomaly pattern. This suggests that applying normal station corrections removes desirable information from the inversion solution. Synthetic modeling indicates that strong velocity perturbations in the unconsolidated sediments, if they exist, can influence the uppermost, Paleozoic portion of the P wave velocity solution but have little effect on deeper portions of the inversion volume. Smearing effects in the S-wave velocity models are more prominent and can affect deeper portions of the velocity model. Examination of the real inversion results suggests that smearing from velocity anomalies in the unconsolidated sediments is, at most, a second order effect. The sediment correction is made using the sediment thickness map and simple velocity versus thickness relationship determined by Bodin et al. (2002). When used to correct for the effects of the sediments, this information produces a reasonable velocity solution in the sense that changes in the velocity anomaly magnitudes yield realistic Vp/Vs ratios throughout the inversion volume. The sediment correction also appears to remove useful information from the inversion solution but is an improvement over removal of normal station corrections for the P wave solution. There is no evidence that the sediment correction is removing smearing effects produced by velocity perturbations in the unconsolidated sediments. Future detailed maps of sediment thickness and more detailed specification of velocity variations could be used to remove second order effects of the unconsolidated sediments on local earthquake tomography solutions.

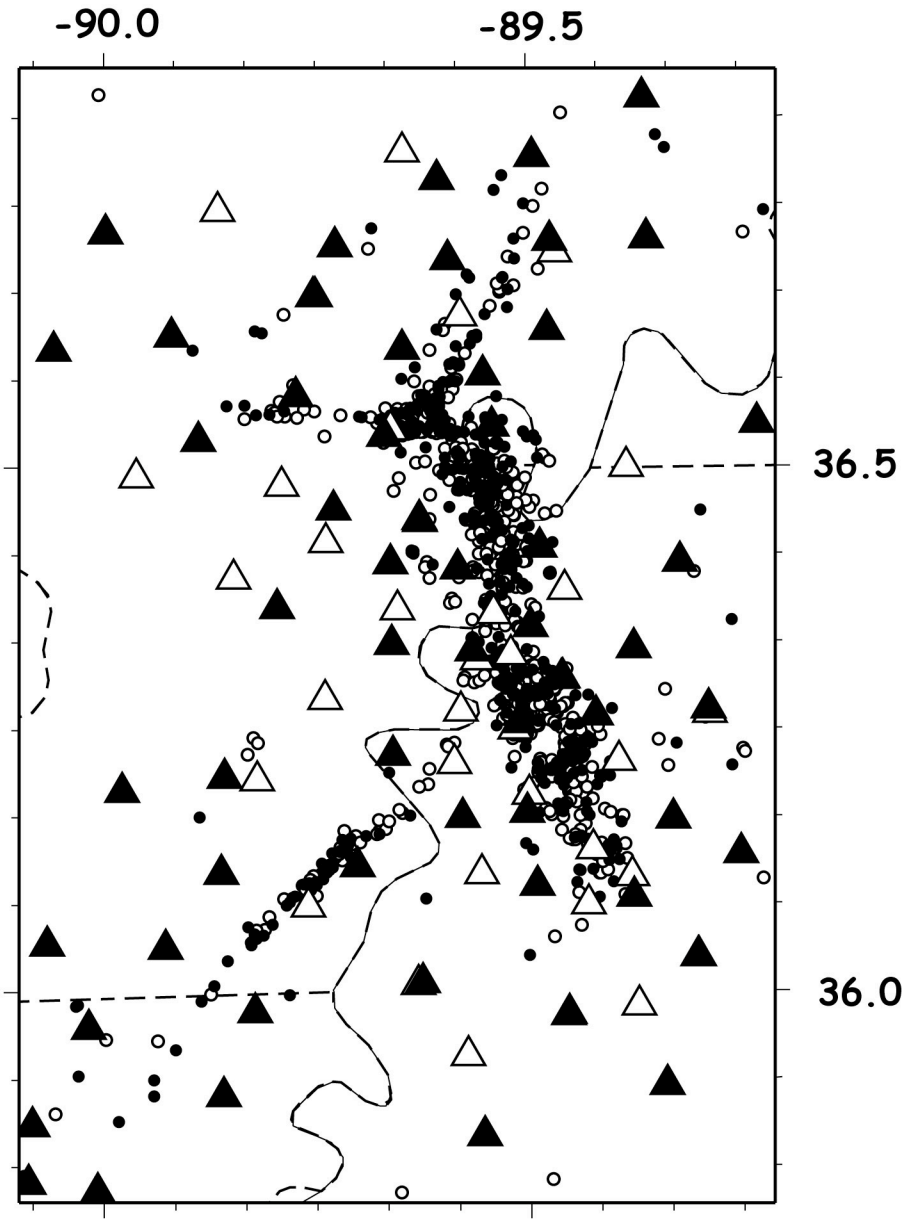

Figure 2.1 Stations (triangles) and earthquakes (circles) used in determination of the effects of the unconsolidated sediments on local earthquake tomography and in the tomographic inversion discussed in section 3 below. Dark symbols CNMSN stations and events; white symbols PANDA stations and events.

3. Higher Resolution Velocity Images for the NMSZ

Background

Detailed Vp and Vs models and Vp/Vs ratios are determined for a major portion of the NMSZ using arrival times recorded by the New Madrid seismic network and Portable PANDA stations. We perform a simultaneous inversion for P and S wave velocities and hypocentral locations. Block size is reduced to 2x2x2 km, yielding a more detailed tomographic image of the upper portion of the crust in than is found using the tomoDD method. The tradeoff is acceptable resolution extends over a smaller portion of the inversion volume.

Data and Tomographic Method

The data and method of analysis that we use in this study are the same as those used in the determination of the effects of the unconsolidated sediments on tomography results discussed above. The 1-D starting model is given in Table 1.1.

Resolution

Synthetic tests

We test resolution within the inversion volume by inverting many synthetic data sets constructed for the source-receiver geometry shown in Figure 2.1. Spike tests, consisting of high or low velocity anomalies confined to one block, and checkerboard tests are used to determine appropriate block size and smoothing parameters, respectively. Checkerboard tests are also used to determine the degree of horizontal and vertical smearing of velocity anomalies within the inversion volume. Synthetic times are calculated using an analytical, 3D ray tracing algorithm (Abers and Roecker, 1991) to provide a data set that is not dependent upon the finite difference method of determining travel times used in the Benz inversion method. Differences between synthetic travel times computed using the analytical method and the finite difference method are less than 0.05 s for both P and S waves and result in velocity models with comparable resolutions. Gaussian noise with zero mean and 0.02 and 0.04 s standard deviation is added to the computed P- and S-wave travel times, respectively.

The spike tests indicate that anomalies placed within blocks with dimensions of 2x2x2 km or greater can be recovered although there is significant smearing due to the smoothing constraints applied. Results are described for a checkerboard synthetic model consisting of alternating ±10% velocity anomalies located in squares with horizontal dimensions of 8 by 8 km. Squares are separated by 4 km wide regions of normal velocity. This synthetic model best represents the spatial extent and magnitude of velocity anomalies resolved using the real travel time data and is used to determine the optimal smoothing parameters and LSQR steps used in the inversion of the real travel times. Excellent recovery of the checkerboard anomalies is obtained when it is placed just below the LVL, in the depth range 4.65 to 10.65 km; maximum recovery occurs in both the P- and the S-wave velocity solutions over the depth range 4.65 to 8.65 km within the portion of the inversion volume containing Reelfoot fault seismicity. Recovery is still good in the depth range 8.65 to 10.65 km but maximum anomaly magnitude is reduced to

±7%. Vertical smearing of high velocity anomalies into the LVL is less than 3% except in a small portion of the layer corresponding to the northern portion of the Reelfoot fault. Horizontal smearing within the checkerboard is most obvious in the NW-SE and NE-SW directions away from Reelfoot fault seismicity and the degree of smearing is similar in the Vp and Vs solutions. In particular, smearing occurs along the trend of the CG-BA fault. Recovery of checkerboard anomalies confined to the layer located above the LVL (depth range 0.65 to 2.65 km) is comparable to that determined for the depth range 4.65 to 6.65 km with very little vertical smearing (<±2.5%) into the LVL.

Smearing is more problematic for velocity anomalies confined to the LVL (2.65 to 4.65 km). Smearing in both the Vp and Vs solutions is greatest in the layer directly above the LVL and produces anomalies reaching 7% in the SE portion of the Vs model (southern portion of the Reelfoot fault). Resolution within the LVL is poor; maximum anomaly magnitude is 4% and occurs in the SE portion of the checkerboard. Resolution within the LVL improves when the checkerboard is extended to include the layer above the LVL, the layer below, or both. However, when the checkerboard is placed in the LVL and the layer below, vertical smearing into the layer above the LVL is intensified.

Another, more complex synthetic model is provided by the restoring resolution test (Zhao et al. 1992) in which P- and S-wave travel times produced by inverting real data are used as synthetic times. Travel times through the final Vp and Vs solutions determined in this study are used as initial input data in the inversion program. The resulting Vp and Vs solutions are very similar to the real solutions, although reduced in magnitude due to the smoothing constraints used in the inversion. Major features in the real inversions are recovered, particularly those associated with the Reelfoot fault. In other portions of the inversion volume, input anomalies ≤ ± 2% are not recovered with fidelity.

The synthetic tests indicate that resolution is highest in the depth range 4.65 to 8.65 km. Anomalies present in the LVL will have reduced magnitudes and will be smeared into the layer above.

Real data

Raypath coverage maps provide a rough estimate of resolution. An accumulated raypath length of >25 indicates that a block is traversed by more than ~10 rays. The maps indicate the best sampled portion of the inversion volume but are not always useful indicators of smearing. For example, raypath coverage is high along the CG-BA fault but smearing results because the raypaths arrive within a narrow azimuth range. Raypath coverage is very similar for the Vp and Vs solutions within the central portion of the inversion volume corresponding primarily to the Reelfoot fault.

V_p/V_s ratios

Vp/Vs ratios are determined by direct division of absolute Vp values by absolute Vs values in that portion of the inversion volume where resolution and ray path coverage for both solutions are similar. This is dictated by the Vs solution, as is evident from the raypath coverage plots.

Results

Inversion results for uncorrected P- and S-wave travel times are shown in Figure 3.1 along with Vp/Vs ratios. Velocity anomalies within each layer are expressed as percent change from the starting 1-D model and only earthquakes that occur within each layer are plotted. The scale used in Figure 3.1, ±6%, does not span the complete range of anomaly magnitudes but allows clear recognition of features that persist through most of the inversion volume. Maximum reduction in RMS residual is about 25% for both the Vp and Vs solutions. This moderate reduction in RMS is expected because the initial RMS values after relocation in the starting 1-D velocity model are small (0.11 s).

Vp and Vs solutions

Very small (+1%) velocity anomalies are present in the top, unconsolidated sedimentary layer. Synthetic modeling and similarity with anomalies resolved in the layer below suggest that they are the result of vertical smearing and will not be investigated further. Often, anomalies with the same sign (either positive or negative) are present in the same place in both the Vp and Vs solutions indicating that there is minimal tradeoff between the velocity solutions. As anticipated from the synthetic checkerboard tests, velocity anomalies have greatest magnitude in the layer above the LVL (0.65 – 2.65 km) and are subdued in the LVL. In general, the CG-BA fault separates high velocity material to the west from low velocity material to the east. This is most evident at depths below 4.65 km in the Vp solution.

There are several distinct anomalies that extend vertically through most or all of the inversion volume. These anomalies are labeled *A* through *G* and are plotted on the shallowest layer of the Vp solution in Figure 3.2. In some instances, the anomaly magnitudes fall below resolution limits as indicated by the synthetic tests but the persistence of these features warrants identification. *A* through *E* are high velocity features that are present throughout most or all of the Vp solution. *A*, if present below 6.65km, is not resolved due to limited raypath coverage. *A* through *E* can be observed in the shallowest layer of the Vs solution but the magnitudes of *B* and *C* do not exceed 2%. Another high Vs anomaly, labeled *F* in Figure 3.2b, extends vertically throughout the Vs solution. *F* is plotted on the Vp solution in Figure 3.2 but is easily seen in the Vs solution in Figure 3.1. Where resolvable, *A* through *E* are associated with high Vp/Vs ratios.

At depths below 4.65 km in the Vs solution, high velocity anomalies are associated with the entire northern portion of the Reelfoot fault and individual features *A* through *C* cannot be distinguished. In certain portions of the inversion volume below 4.65 km, high Vs anomalies (e.g. *F*) correspond to low P wave velocity anomalies resulting in low Vp/Vs ratios. Regions containing the most prominent low Vp/Vs ratios are labeled *G* in Figure 3.2 and correspond to the northern portion of the Reelfoot fault and the two northernmost arms of seismicity extending west and northeast (see Figure 1). In general, all of the seismicity arms are associated with low Vp/Vs ratios at depths below 4.65 km (Figure 3.1).

A prominent low velocity anomaly labeled *H* is present throughout the inversion volume in both the Vp and Vs solutions. This feature is associated with a high Vp/Vs ratio.

Another persistent low velocity anomaly labeled *I* can be observed throughout most of the inversion volume in both solutions. In general, this feature is associated with a low Vp/Vs ratio. Feature *J* is located at the extreme edge of resolution and is included only because it corresponds to the southern termination of the Reelfoot fault. *J* is associated with a high Vp/Vs ratio but diminished resolution in the Vs solution makes this calculation suspect.

Cross-sections

A series of cross sections shown in Figure 3.3 illustrates the relationship between resolved velocity structure and relocated hypocenters. Vp and Vs anomalies are shown in Figures 3.3a and b and Vp/Vs values are shown in Figure 3.3c. Cross section locations are plotted on the Vp solution for the depth range 4.65-6.65 km (Figure 3.3b). Hypocenters located at a distance of 1 km or less from each profile are plotted. This small distance is equivalent to the hypocenter horizontal error prior to relocation in the inversion and properly associates hypocenters with velocity structure. Cross-sections 1 and 2 correspond to the trend of the northernmost arm of NMSZ seismicity. Cross-section 3 is associated with the E-W trending arm located at the northern end of the Reelfoot fault. The remaining sections pass through the Reelfoot fault.

The northernmost arm of the NMSZ appears to consist of two parallel trends of seismicity. Cross-sections 1 and 2 do not share common hypocenters and depict two independent groups of earthquakes that could be associated with separate faults. Two separate faults can also be seen in cross-section 3 where this slice crosses 1 and 2. Cross-sections 1 though 3 illustrate a relationship between the sign of the velocity anomalies and the hypocenters that is found for the entire northern portion of the Reelfoot fault; hypocenters are associated with low Vp anomalies and high Vs anomalies. As a consequence, hypocenters are associated with low Vp/Vs ratios. This relationship between velocity anomalies and hypocenters is particularly evident in cross-sections 4 and 5 (Figures 3.3a and c). Here, low Vp and high Vs anomalies are present in the footwall of the Reelfoot fault. The relationship between hypocenters and low Vp and high Vs anomalies is not evident in the southernmost portion of the northern Reelfoot fault (E-W cross-section 6). Here, the fault trends almost N-S and the dominant velocity feature is a region of low Vp and Vs anomalies in the hanging wall.

Cross-section 7 trends along the CG-BA fault and illustrates the velocity structure associated with the intersection of this fault and the Reelfoot fault. The intersection is marked by the presence of high Vp and Vs anomalies in the upper 6 km of the inversion volume. The distribution of hypocenters along the southern Reelfoot fault is complex. Hypocenters in cross-section 8, located a few km south of the intersection of the CG-BA fault, appear to delineate a fault dipping to the SW. However, hypocenters in cross-sections 9, 10, and 11 display a completely different pattern and an obvious return to the SW dipping fault plane is not observed until the location of cross-section 12. Seismicity in cross-section 9 appears to cluster into two groups. Individual clusters of seismicity may also be present in cross-section 10, resulting in the flat to NE dipping appearance of the fault zone. Seismicity in cross-sections 8 through 12 is associated with a prominent

low Vp anomaly and an associated but weaker low Vs anomaly (anomaly *I* in Figure 3.2a). As a result, the seismicity is associated with low Vp/Vs ratios (Figure 3.3c).

Synthetic modeling

Velocity models that represent ideal, geological entities, such as high velocity intrusions, are created and synthetic travel time data sets calculated to investigate the spatial response of the inversion algorithm. We pose a number of simple, geological hypotheses to determine if they are consistent with the final inversion results (Figures 3.1 – 3.3). This exercise is a refined resolution test that incorporates geological knowledge to investigate velocity anomaly magnitudes and spatial smearing. In the following, a "synthetic velocity model" is one of these ideal models for which we calculate a synthetic arrival time data set using the source-receiver geometry shown in Figure 2.1. The "real" solution pertains to our final tomographic inversion result shown in Figures 3.1 – 3.3.

We address the following questions: 1) How shallow is the top of the resolvable portion of each intrusion? 2) Can the intrusions be modeled using geologically reasonable absolute Vp and Vs values? 3) Is feature *F* observed in the S wave velocity solution produced by smearing of *D* and *C* or does it require the presence of additional high Vs material? 4) Do features *A – D* smear together to produce the prominent crescent-shaped high velocity anomaly observed at depths exceeding 4.65 km in the Vs solution? The real solutions shown in Figures 3.1 – 3.3 do not provide unique, absolute velocity values because the magnitude of the imaged velocity anomalies is dependent upon the amount of smoothing used in the inversion. Synthetic modeling of the Vp and Vs anomalies independently will also lead to non-unique absolute velocity values. The Vp/Vs ratio is less affected by smoothing in those portions of the inversion model where Vp and Vs resolution is comparable and, requiring the synthetic models to match observed ratios as well as velocity anomalies provides constraint on absolute velocities (White et al., 1992; Holbrook et al., 1988). All synthetic models are generated using the same source-station geometry, starting model, and smoothing parameters used in the real data inversion.

We begin by generating a synthetic model for feature *D*, the most prominent velocity anomaly. We construct an initial Vp and Vs model through a trial and error process that reproduces *D* in the depth range 4.65 to 6.65 km, the range with maximum resolution and minimum vertical smearing. The Vs anomaly associated with *D* in this depth range is obscure. (The prominent velocity high is feature *F*.) Thus, the velocity model is constructed by matching the observed Vp anomaly and Vp/Vs ratio. Several model horizontal dimensions are tested as well as a wide range of absolute velocity values. A model with horizontal EW-NS dimensions of 12x8 km produces the best match with the dimensions of *D* regardless of the absolute velocity values tested. The model that best matches observations within this layer has absolute Vp and Vs values of 6.60 and 3.75 km/s, respectively. Changing Vp by more than ± 1% produces a poor match to observations and we are unable to reproduce the observed anomalies by requiring the Vs anomaly to be zero. This model is then extended up into the LVL keeping the absolute Vp and Vs values fixed. These velocities produce large anomalies in the LVL that are smeared into the layer above and, to a lesser extent, into the layer below. In order to match observed anomalies in the layer above the LVL, we must extend the synthetic

model into this layer (i.e. into the depth range 0.65 to 2.65 km). Minor adjustments to the velocity values in the layers below the LVL must be made to account for vertical smearing.

Features *B*, *C*, and *E* are modeled by assuming that they are produced by the same material producing *D*. Resolution for feature *A* decreases rapidly with depth and is not modeled. The primary objective is to determine if features *B*, *C*, *D*, and *E* merge in the Vs solution at depths exceeding 4.65 km. A close fit between synthetic Vp anomalies and Vp/Vs ratios for *B*, *C*, and *E* and observed values is obtained when the horizontal EW-NS dimensions of the anomalies are 6x6 km, 4x6 km, and 4x12 km, respectively. Minor adjustments to the velocity values used to model *D* are needed to model *B* and *C*, as indicated in Table 4.1. Anomaly *E* requires a gradient in Vp which is modeled as two blocks with Vp higher in the northern portion of *E* than the southern portion. Unlike *D*, the modeled features *B*, *C*, and *E* extend into the LVL but no shallower. The synthetic model solutions can be compared to those obtained for the real data shown in Figure 3.1b. The match between synthetic and real Vp solutions is good for this layer and for the remaining layers in the depth range 0.65 to 8.65 km. The same can be said for the Vp/Vs ratios. The synthetic Vs anomalies remain distinct and do not smear together to produce the large high velocity feature *F* or the crescent shaped high velocity pattern observed in the inversion of real data. This result suggests that additional high Vs material must be present in between the intrusions.

Feature *F* is prominent below depths of 4.65 km and contains high Vs and normal to slightly low Vp material. This combination results in a Vp/Vs ratio as low as 1.61. Feature *F* can be modeled successfully by increasing Vs in between anomalies *C* and *D* by 6.5% in the depth range 4.65 to 8.65 km and by 14% in the LVL. Restricting the anomalously high Vs material to the depth range 4.65 to 8.65 requires a 14% increase in Vs and produces an unacceptably low Vp/Vs ratio of 1.57. The successful synthetic model is a close match for the portion of the inversion volume modeled. In a similar fashion, increasing Vs in between features *B* and *C* creates low Vp/Vs ratios, as observed in the solutions for the real data, and creates the top portion of the crescent shaped, high Vs anomaly apparent at depths exceeding 4.65 km. Anomalously low Vp and anomalously high Vs anomalies also produce other regions displaying low Vp/Vs ratios, represented by *G* in Figure 3.2. Vs anomalies in all regions labeled *G* must exceed 5% in order to match observed values but can be confined to basement rocks (i.e. to rocks below the LVL).

We begin modeling anomaly *H*, the prominent low velocity anomaly observed in the Vp and Vs solutions, by matching Vp and Vs anomalies in the depth range 4.65 to 6.65km. This is accomplished using a rectangular model with horizontal EW-NS dimensions of 6 by 12 km containing Vp and Vs anomalies of –6 and -9%, respectively. The low velocity material causes smearing into the layers above, as suggested by the checkerboard tests, but not to the extent observed in the real solutions; confining the Vp and Vs anomalies to depths below the LVL cannot reproduce the negative anomalies observed in the LVL or the top layer. Similarly, extending the low velocity material into the layers above and below does not result in a good match between observed and synthetic anomalies. In

fact, reasonable low velocity material in the depth range 4.65 to 6.65 km still produces high velocity material in the LVL above. Our successful models for *H* require velocity reductions of 4 to 6 % throughout the depth range 0.65 to 8.65 km. The same conclusion applies to low velocity anomaly *I*.

Interpretation

We are able to model features *B-E* using geologically reasonable absolute Vp and Vs values. Although it is not possible to use the velocity values to specify a unique rock composition, we can narrow down the possibilities as has been done in previous studies (Holbrook et al., 1988; White et al., 1992; Christensen and Mooney, 1995; Christensen, 1996; Chevrot and van der Hilst, 2000; Zhang et al., 2008). Based upon tables of Vp, Vs, and Vp/Vs for various rock types provided by Christensen (1996), Zhang et al. (2008), and Brown et. al (2008), the composition of *B-E* falls closest to diorite and diabase, both intrusive igneous rocks.

Rocks in between features *C* and *D* (feature *F*) and in other regions labeled *G* in Figure 3.2 have high Vs but normal to slightly low Vp values relative to the starting model. Compositionally, this result can be met by quartz-rich rocks. An estimate of the amount of quartz present can be obtained using a plot of % silica versus Poisson's ratio present in Christensen (1996) (with minor adjustments to 200 MPa pressure). For our observed Vp/Vs ratio of 1.62, the rocks must contain about 80% silica (weight percent). If the basement rocks in between the intrusions are granites, then the normal amount of silica is about 72% (Christensen, 1996; Blatt and Tracy, 1997). If we attribute the increase in silica content to the presence of quartz alone, rather than an increase in other silica minerals such as feldspar, then the 80% silica content suggests that these rocks contain approximately 25 to 30% quartz, in addition to the quartz commonly found in granite (about 20%) (N. Christensen, personal communication). The presence of granitic basement rocks is indicated by geological evidence (Thomas, 1985; Dart and Swolfs, 1998) and potential field studies (Hildenbrand et al., 1996). A rough estimate for the Vp and Vs values for granitic rock with 80% silica can be obtained using velocity and % silica values for quartzite and granite provided by Christensen (1996). Assuming a linear relationship between velocity and % silica, the expected Vp and Vs values are 6.12 and 3.80 km/s, respectively. This translates into Vp and Vs anomalies of -1 and 6.5%, respectively, in agreement with the tomographic solution for depths exceeding 4.65 km (Figure 3.1).

In addition to lithologic variations, seismic velocities and Vp/Vs ratios are influenced by porosity, pore pressure, pore aspect ratio, and fluid or gas saturation (O'Connell and Budianski, 1974; Dvorkin et al., 1999; Zhao and Negishi, 1998; Nakajima et al., 2001; Takei, 2002; Moretti et al., 2009). Can the low Vp/Vs ratios observed in the regions labeled *G* in the NMSZ be attributed to the presence of fluids or gas in fractured rocks? Methods to determine the aspect ratio of saturated pores and the volume fraction of liquid can be found in Takei (2002) and Nakajima et al. (2001). Analyses by both Takei (2002) and Nakajima et al. (2001) indicate that low Vp/Vs ratios can be attributed to the presence of water- or gas-filled, high-aspect ratio cracks. However, the low Vp/Vs ratios are produced by decreases in both Vp and Vs, with Vp decreasing more than Vs. Clearly,

this does not apply to our situation where low Vp/Vs ratios are produced by a small decrease in Vp and a large increase in Vs. The low Vp/Vs ratios in regions labeled *G* are most logically attributed to variations in rock composition.

Regions labeled *H* and *I* in Figure 3.2a cannot be modeled easily by invoking changes in lithologic properties and most probably are due to the presence of fluids. In fluid filled rock volumes, particularly those with low aspect ratio cracks, increasing pore pressure can reduce Vp and Vs but has a stronger influence on Vs, resulting in an increased Vp/Vs ratio (Christensen, 1989; Takei, 2001, Nakajima et. al, 2001). Anomaly *H* extends to a depth of 9 km (see cross section 5, central high Vp/Vs anomaly), suggesting that fluids would likely be at high pore pressures. Vp and Vs are reduced by approximately 3 and 5.5%, respectively, while Vp/Vs is increased to 1.78. These values can be used in a plot of the fractional change in Vp and Vs, $d\ln Vs/d\ln Vp$, versus aspect ratio computed by Takei (2001) for gas, water, and magma at several depths to determine what conditions most likely exist in region H. For our conditions, $d\ln Vs/d\ln Vp = 1.83$ and anomaly *H* can be attributed to the presence of water-filled, low aspect ratio cracks (ratio of about 0.0030 to 0.004) with about 1 to 1.5% liquid volume fraction. Similar results are obtained using the analysis of Nakajima et. al (2001). A different set of conditions exist in region *I*. Here, Vp and Vs are both reduced but Vp has the greatest reduction, resulting in a low Vp/Vs ratio (see cross sections 9 and 10, Figure 3.3). Vp and Vs are reduced by about 5.5 and 2.5%, respectively, and Vp/Vs decreases to 1.67. According to the analysis of Nakajima et. al (2001), region *I* probably contains a low (approximately 3%) volume fraction of water-filled cracks with high aspect ratios. The analysis of Takei (2001) also indicates the presence of high aspect ratio cracks but filled with gas.

Discussion

Several interesting features are imaged in the Vp and Vs solutions that could have bearing on why and where NMSZ seismicity is occurring. Of particular interest is the presence of intrusions, the very low Vp/Vs ratio values associated with the arms of seismicity, and the low velocity region associated with the southern portion of the Reelfoot fault. As a further test of the reliability of our results, Vp and Vs models incorporating the data set used in this study are derived using the inversion method tomoDD (Zhang and Thurber, 2003). Results of the tomoDD inversion are given in Dunn (2009). Briefly, the tomoDD solution is not as detailed as the models presented here but major features such as *D*, *F*, and *H* are resolved. Most importantly, low Vp/Vs ratios are imaged that correspond to the Vp/Vs lows found in our study. The two inversion results are very similar when the block size in our study is increased to match the smallest node spacing (5km) in the tomoDD model grid. A recent joint inversion of teleseismic and local P-wave arrival times by Zhang et. al (2009) has limited resolution in the upper crust and the solution cannot be compared in a meaningful way to our results.

Features *A* through *E* imaged in our study are interpreted to be high velocity intrusions. Features *A* through *D* are located approximately on the northwest boundary of the Reelfoot graben, as mapped by regional-scale magnetic anomalies (Hildenbrand and Hendricks, 1995) while *E* is located within the graben. *D*, the most prominent and shallowest intrusion, is located about 12 km east of positive gravity and magnetic

anomalies associated with the Malden pluton, one of several mafic intrusions mapped along the northwest boundary of the Reelfoot graben by Hildenbrand and Hendricks (1995). The Malden pluton is by far the smallest of the mapped intrusions and features *A-E*, which are smaller than the Malden pluton, are not discernable features in the potential field maps. Magnetic anomalies corresponding to features *B-D* are observed in a map created from a high-resolution aeromagntic survey flown over the northern portion of the NMSZ (Hildenbrand et al., 1992). Here, the grid spacing for the map is 0.1 km as opposed to 1 km for the regional maps shown in Hildenbrand and Hendricks (1995). Our anomaly *D* corresponds to anomaly F in Hildenbrand et al. (1992) and appears to be unassociated with the Malden pluton. Our anomalies *B* and *C* correspond to two peaks in anomaly E in Hildenbrand et al. (1992); anomaly E is associated with a SE extension of the large Bloomfield pluton. The 40 km wide Bloomfield pluton is located to the north of the Malden pluton and appears as a prominent high in both the regional-scale magnetic and gravity maps produced by Hildenbrand and Hendricks (1995). Although the age of the Bloomfield pluton may be pre-Late Cambrian, the remaining plutons located along the margin of the graben were probably emplaced during a reactivation of the Reelfoot rift in late Cretaceous time (Hildenbrand, 1985).

Previous studies point out a distinct relationship between earthquake occurrence and the location of mafic plutons emplaced along the flanks of the Reelfoot rift; earthquakes occur around the edges of the plutons and avoid the pluton interiors (Hildenbrand and Hendricks, 1995; Hildenbrand et. al, 2001; Ravat et. al, 1987). This relationship is most striking for the Malden and Bloomfield plutons and is attributed to far-field stress concentration due to the higher elastic stiffness and strength of the intrusions (Hildenbrand and Hendricks, 1995; Hildenbrand et. al, 2001). Seismicity also occurs in between the smaller plutons imaged in our study. Note in Figure 3.2b that epicenters lay in between intrusions *C* and *D*, *C* and *B*, and *C* and *A*. The presence of even small intrusions appears to exert a controlling influence on seismicity. Feature *J* in Figure 3.2a could be an intrusion influencing the southern termination of the Reelfoot fault. Unfortunately, we do not have enough resolution in our current model to explore this further.

We attribute the low Vp/Vs ratios associated with the major strike-slip arms of seismicity in the northern portion of the NMSZ to the presence of quartz rich rocks located in between intrusions *A – D*. These rocks occur within the Precambrian granitic basement and could have been present prior to the emplacement of the intrusions. Alternatively, the rocks could host quartz veins produced as a result of thermo-tectonic processes associated with rift reactivation and intrusion emplacement in the Cretaceous. Synthetic modeling results for feature *F* suggest that the high Vs material extends into the LVL (Elvins shale), supporting the presence of quartz-rich veins rather than preexisting high Vs Precambrian basement rocks. Generation of abundant quartz veins is often associated with tectonic processes involving the release of fluids. These include the release of hydrothermal fluids by regional metamorphic processes during transpressive tectonic events (Jia and Kerrich, 2000; Kerrich and Feng, 1992), magmatic fluid release during crystallization of silicic magmas (Boiron et al., 1996), and late-stage hydrothermal alteration along strike-slip faults (Mark et al., 2004). As an example, Cheong (2002)

describes quartz veins in low-grade metamorphic rocks within shear zones in Nevada that formed at depths of 5 to 10 km due to tectonically induced fluid flow. Quartz is a weak mineral and is used to develop strength versus depth curves (brittle-ductile transition) for the crust (Meissner and Strehlau, 1982; Chen and Molnar, 1983). If abundant quartz is responsible for the low Vp/Vs ratios associated with the northern NMSZ strike slip arms of seismicity, then ductile behavior (creep) could be facilitated at depth resulting in shear strain loading and the generation of earthquakes in the crust above. Possible evidence for creep is provided by recently discovered non volcanic tremor at a depth of approximately 20 km in the NMSZ (Langston et. al, 2009b).

The higher resolution magnetic anomaly map of Hildenbrand et. al (1992) does not extend over our anomaly *E*. This feature is located in the center of an arcuate, regional-scale, magnetic high located within the Reelfoot graben that has been interpreted as a ring-dike complex (anomaly O in Hildenbrand and Hendricks, 1995). Anomaly O is shaped like a 90º clockwise rotated "C". The eastern arm of O is clearly associated with Reelfoot fault seismicity and has been modeled as an intrusion within the Precambrian basement rock by Rabak (2009). Depths to the top of the intrusion range from 3 to 6 km. The eastern arm of the crescent shaped, high Vs anomaly apparent at depths exceeding 4.65 km in our tomographic solution corresponds with the steep eastern edge of O as far south as the intersection of the CG-BA fault with the Reelfoot fault. Anomaly O also diminishes in amplitude south of this intersection. Two observations suggest that the intrusion producing anomaly O is less mafic than intrusions emplaced along the margins of the Reelfoot graben. First, anomaly O does not have a positive gravity signature. Second, Reelfoot fault seismicity occurs almost exclusively within the intrusion rather than in surrounding rock, as is the case for the Malden and Bloomfield plutons (Ravat et. al, 1987) and for intrusions *A* - *D* found in this study. We suggest that the intrusion producing anomaly O is primarily felsic in composition and thus does not have a strong density contrast with surrounding basement rock. The steep eastern edge could contain a high percentage of quartz manifesting as high Vs anomalies in our inversion solution. Careful examination of earthquake hypocenters indicates that most occur in the portion of the intrusion that corresponds to the high Vs values observed in our solution (see cross sections 4 and 5, Figure 3.3). Unlike mafic intrusions such as the Maldon pluton, the quartz-rich part of anomaly O could represent a relatively weak portion of the crust capable of hosting seismic activity.

Region *H* in our study is located in the central portion of anomaly O and is associated with large magnetic highs and a distinct but small amplitude gravity low (Rabak et. al, 2009). We suggest that *H* contains high pore pressure, water-filled, low aspect ratio microcracks. Low Vp and high Vp/Vs regions, such as *H*, are associated with active fault zones (Michelini and McEvilly, 1991; Eberhart-Phillips et. al, 1995; Thurber et. al, 2003; Moretti et. al, 2009) and volcanic regions (Zhao and Negishi, 1998; Zhao et. al, 2002; Nakajima et. al, 2001) and are often attributed to overpressured water. Recent studies near Parkfield are particularly revealing because they involve high resolution velocity images used to site the San Andreas Fault Observatory at Depth (SAFOD). Thurber et. al (2003) determined detailed 3D Vp and Vp/Vs structure around the SAFOD site and found high Vp/Vs zones adjacent to the San Andreas fault and in the hypocentral region

of the 1966 Parkfield main shock. The high Vp/Vs zones range in depth from 2 to 9 km and are interpreted to be fluid rich. Interestingly, the high Vp/Vs zones are virtually aseismic, indicating that fault slip occurs as either creep or via dynamic rupture in larger earthquakes such as the 1966 event (Thurber et. al, 2003). The 1995 Kobe mainshock hypocenter is also located in a distinct region characterized by low Vp and Vs and high Vp/Vs. The anomalous region is attributed to the presence of fluid filled, fractured rocks (Zhao and Negishi, 1998) and is located outside of the aftershock zone. Region *H* in our study is located in the hanging wall of the Reelfoot fault and is virtually aseismic (Figure 3.1 and cross section 5, Figure 3.3). Creep could be occurring here or *H* could be an overpressured volume of rock that provides a source of fluids to the Reelfoot fault. Conceivably, *H* could be the hypocentral region of one of the large 1811-1812 NMSZ earthquakes. According to most reconstructions of the 1811-1812 sequence, *H* lies in between the 02/07/1812 and 01/23/1812 event epicenters (Johnston and Schweig, 1996) but uncertainty in these locations is large and the possibility that *H* is a hypocentral location cannot be dismissed.

Region *I* is also interpreted to be a fluid saturated volume but the low Vp/Vs ratio suggests the presence of high aspect ratio pores rather than flat cracks. Meteoric water is probably the saturating medium although the presence of gas cannot be ruled out. Low Vp/Vs ratios attributed to the presence of water and/or gas are associated with geothermal areas (Julian et al., 1996, 1998), active extension in the Apennines (Moretti et al., 2009), the upper crust below active volcanoes in northeastern Japan (Nakajima et al., 2001), and volcanic activity in southwest Iceland (Tryggvason et al., 2002). These low Vp/Vs regions are, in general, seismically active, as is the case with region *I* in our study. Seismicity associated with region *I* is distinctly different from the other portions of the southern Reelfoot fault. Looking at the cross sections through the southern Reelfoot fault (sections 7-12 in Figure 3.3), we see that the expected SW dip of the fault, as defined by seismicity, is apparent in sections 7, 8, and 12. In sections that traverse region *I*, 9-11, the seismicity becomes diffuse and, in 10, appears to delineate a fault plane dipping to the NE. This apparent dip is probably an artifact produced by several individual earthquake swarms. Swarms are documented in this portion of the Reelfoot fault (Xie et al., 1997; Xie, 2001; Bisrat et. al, 2008) and are attributed to localized increased pore fluid pressures (Xie et al., 1997; Bisrat et. al, 2008).

Hydrologic and mineralogical evidence for present and past high pore pressures in the upper 5 km of the Reelfoot Rift crust is found in well logs and cores (McKeown and Diehl, 1994). The principle evidence for excess fluid pressures is artesian flow from aquifers in Paleozoic rock and circulation of water from great depths is indicated by chemical and thermal properties of water samples. Numerical modeling by Wolf et. al (2005) demonstrates that excess pore pressures in the upper 5 km result from gravity-driven flow and can be sustained in a wide discharge area encompassing most of the NMSZ. There is abundant evidence in other parts of the world that fluids, including meteoric water, are present in fault zones down to mid-crustal levels (McCaig, 1988; Stibson, 1994; Boiron et. al, 1996; McCaig et al., 2000; Yonkee et al., 2003; Mark et al., 2004; Imber et al., 2008; Wibberley et al., 2008).

One of the most striking results of our study is the velocity contrast across the CG-BA fault at depths exceeding 4.65 km (Figure 3.1). The contrast in Vp is particularly evident; basement rocks NW of the fault are 4 to 6% faster than rocks located to the SE. Diminishing resolution in the inversion solution prevents us from determining if the velocity contrast extends south of about 36.08º. Assuming that the velocity contrast ends at 36.08º and that the contrast reflects two different rock types juxtaposed by strike-slip motion, the minimum horizontal movement along the CG-BA fault is about 40 km. This seems excessive and is not supported by other geological or geophysical evidence. A much more likely scenario is that the velocity contrast reflects a preexisting structural or lithologic boundary in the Eastern Granite-Rhyolite Provence basement rocks. The low Vp region also appears to be bounded to the SE producing an approximately 30 km wide band of low velocity material (Figure 3.1). This low velocity band extends to the NE, beyond the location of the southern segment of the Reelfoot fault, further suggesting that the low velocity region is a preexisting feature in the basement rather than one that can be attributed to the current mode of faulting. The NE-SW trend of the low velocity band is compatible with the trends of major structural features in the central and eastern U.S. reflecting ancient collisional and extensional events (Thomas, 1991). These observations suggest that the location of the CG-BA fault could be strongly influenced by preexisting basement structure.

Our results may be providing insight into why earthquakes occur in the NMSZ and not in other intraplate fault zones that are also favorably oriented in the present day stress field. Anomalous Vp/Vs ratios are associated with the major arms of seismicity and suggest both compositional and fluid overpressure conditions that could accommodate earthquake occurrence. Numerous intrusions and possibly, preexisting basement structure, appear to control the geometry of the major arms of seismicity. However, we will not know if the features found in our study are unique to the NMSZ or extend to other ancient fault zones until detailed geophysical studies are conducted in presently aseismic regions in the central and eastern U.S. The passage of USArray will afford such an opportunity.

Conclusions

We present detailed 3D images of Vp, Vs, and Vp/Vs for the New Madrid seismic zone based upon inversion of local earthquake arrival times. Resolution is highest for the Reelfoot fault and is adequate to a depth of 8.65 km. The presence of a low velocity layer in the depth range 2.65 to 4.65 km limits resolution in this portion of the inversion volume and amplifies velocity anomalies in the layer above. Several features are imaged that extend vertically through all or most of the inversion volume. A minimum of five mafic intrusions are detected. Four are associated with the NW flank of the Reelfoot rift and one occurs within the rift. Only one intrusion penetrates to depths less than 2.65 km. Relocated hypocenters occur in between the flank intrusions, mimicking the relationship found for NMSZ seismicity and larger intrusions detected in previous studies. Anomalously low Vp/Vs ratios are associated with major arms of seismicity north of the intersection of the Cottonwood Grove – Blytheville Arch fault and the Reelfoot fault. The low Vp/Vs ratios are produced by slightly low Vp and high Vs and are attributed to the presence of quartz-rich rocks. We suggest that the abundant quartz facilitates creep at depth and shear strain loading and the generation of earthquakes in the crust above. Two

regions contain anomalous Vp, Vs, and Vp/Vs ratios that cannot be attributed to variations in rock composition and are probably produced by overpressured fluids. We suggest that a low Vp and high Vp/Vs region associated with the northern portion of the Reelfoot fault contains high pore pressure, water-filled, low aspect ratio microcracks. This region is located on the hanging wall of the Reelfoot fault and is aseismic. Creep could be occurring here or the feature could be an overpressured volume of rock that provides a source of fluids to the Reelfoot fault. We find low Vp, low Vs, and low Vp/Vs associated with the southern portion of the Reelfoot fault in a region that experiences swarm activity. We attribute the anomalous Vp and Vs values to the presence a low volume fraction of water-filled cracks with high aspect ratios. A striking change in Vp occurs across the Cottonwood Grove – Blytheville Arch fault at depths exceeding 4.65 km; basement rocks NW of the fault are 4 to 6% faster than rocks located to the SE. This velocity contrast extends to the NE, beyond the present location of the southern portion of the Reelfoot fault and is interpreted as a preexisting structural or lithologic boundary in the basement rocks.

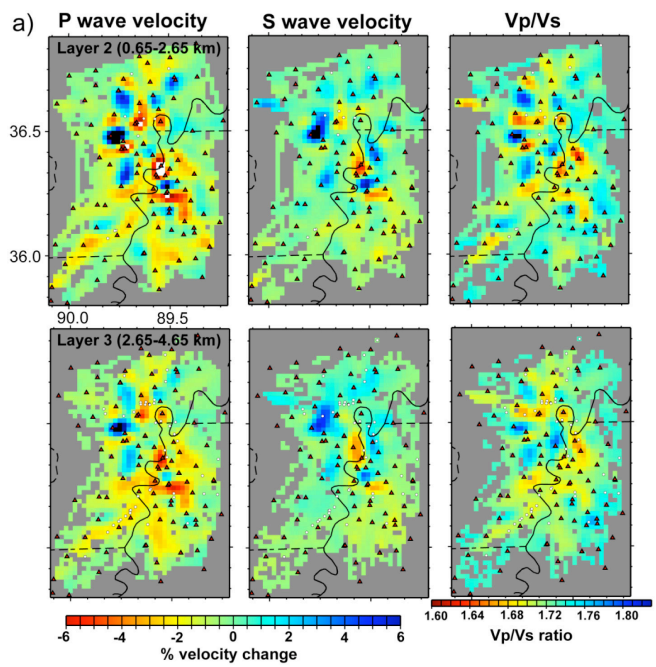

Figure 3.1 Vp (left) and Vs (middle) solutions and Vp/Vs (right) obtained using the real arrival time data. Planar slices are shown in two km increments through the most highly resolved portion of the inversion volume (0.65 to 8.65 km depth). Hypocenters that occur within each depth slice are indicated. P- and S-wave velocity values in percent change relative to the starting model; Vp/Vs shown as absolute values.

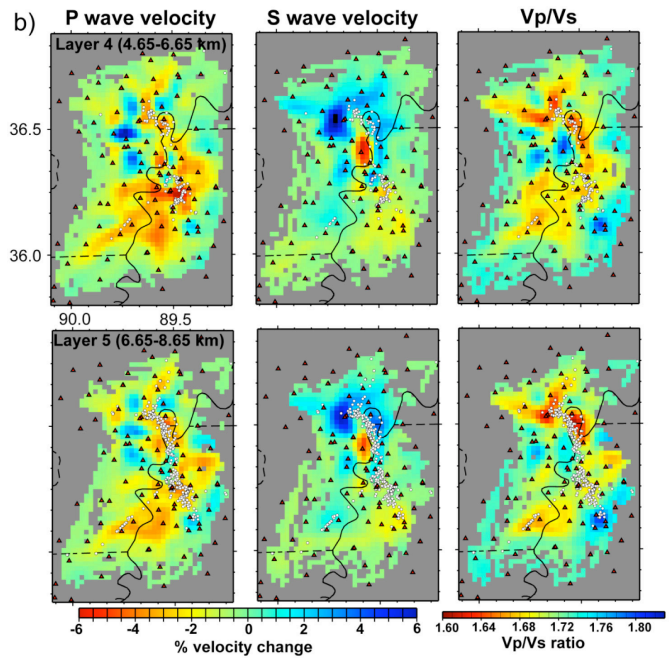

Figure 3.1 continued.

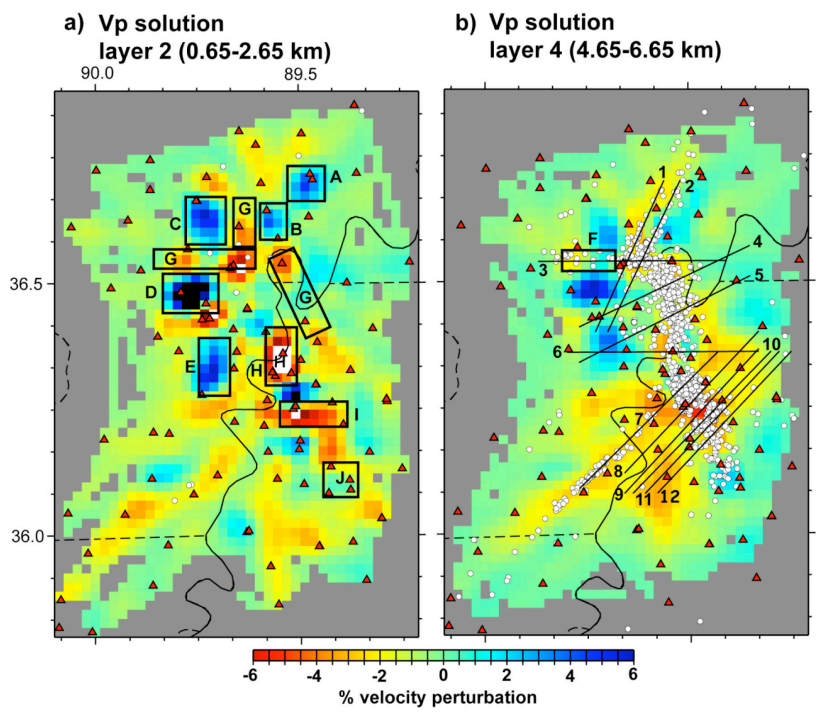

Figure 3.2 a) Major features identified in the velocity inversion plotted on the Vp depth

slice 0.65 to 2.65 km. (F shown in Figure 7b). Features F and G are prominent in deeper portions of the inversion solution. b) Location of cross sections shown in Figure 8 plotted on the Vp depth slice 4.65 to 6.65. All hypocenters are plotted to illustrate the relationship between the cross sections and the relocated hypocenters.

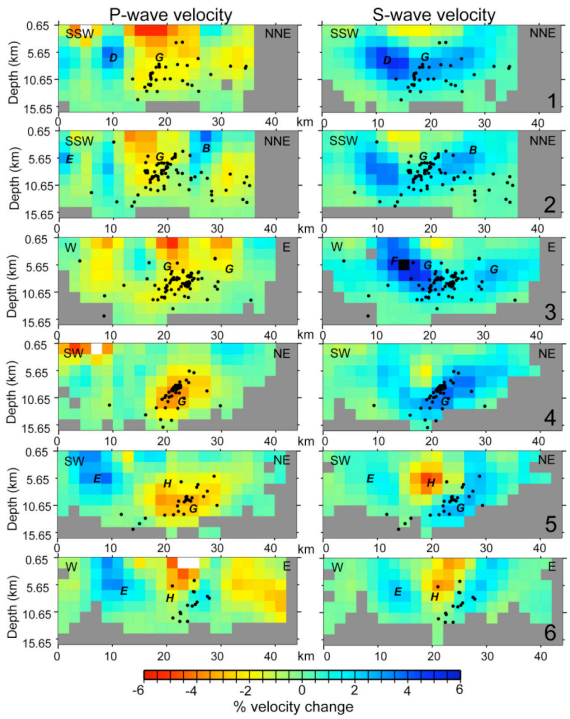

Figure 3.3 a) Cross sections through the Vp and Vs solutions. Cross section locations given in Figure 7b. Vp on the left and Vs on the right. Hypocenters located within one km of each profile are plotted. Letters refer to major features identified in the inversion solutions. Locations of features given in Figure 7a. b) Same as a) for cross sections south of the intersection of the CG-BA fault and the Reelfoot fault. c) Vp/Vs cross sections corresponding to the profiles in a) and b).

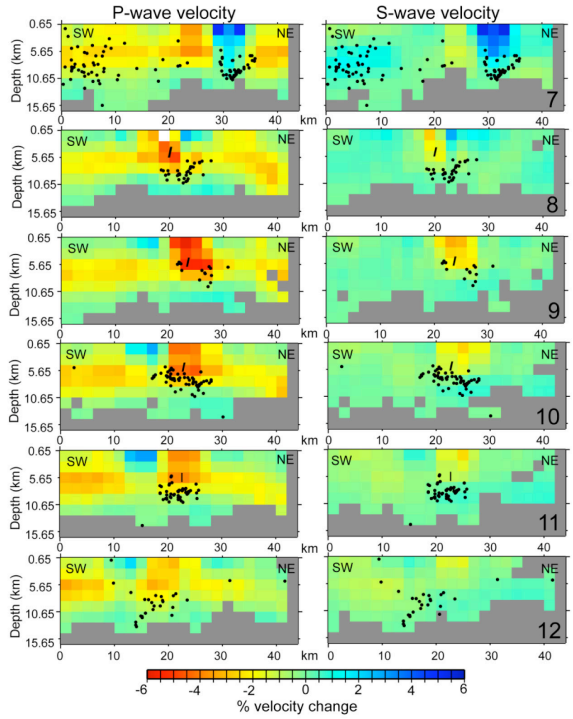
P-wave velocity
S-wave velocity
SW
NE
Depth (km)
0.65
5.65
10.65
15.65
0
10
20
30
40
km
7
8
9
10
11
12
-6
-4
-2
0
2
4
6
% velocity change

Figure 3.3 b)

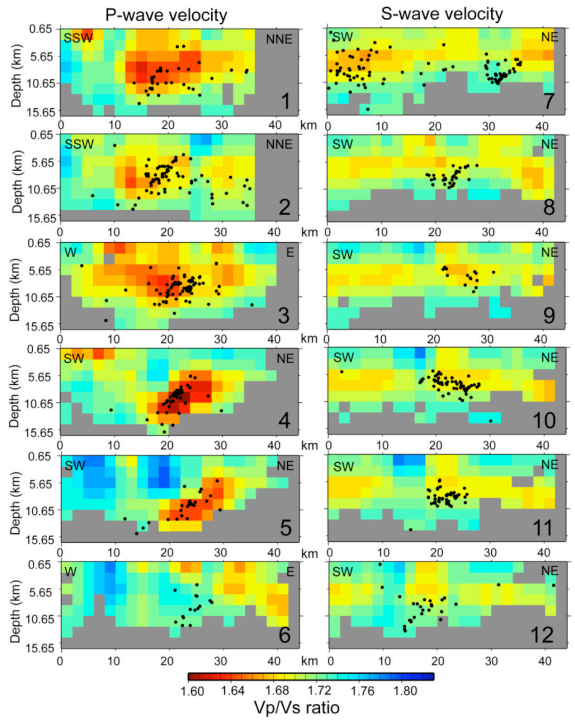
P-wave velocity
S-wave velocity
Depth (km)
0.65
5.65
10.65
15.65
0
10
20
30
40
km
SSW
NNE
SW
NE
W
E
1
2
3
4
5
6
7
8
9
10
11
12
1.60
1.64
1.68
1.72
1.76
1.80
Vp/Vs ratio

Figure 3.3 c)

PUBLICATIONS RESULTING FROM THIS GRANT

Published

Dunn, M. (2009), High resolution earthquake locations and velocity models in the New Madrid seismic zone, Ph.D. Dissertation, The University of Memphis, Memphis, TN, 137pp.

Powell, C.A., and M. Withers (2009), The effects of Mississippi embayment sediments on local earthquake tomography, *Seism. Res. Lett., 80*, 149-158.

Submitted manuscripts

Powell, C., M. Withers, H. DeShon, and M. Dunn, Intrusions and anomalous Vp/Vs ratios associated with the New Madrid seismic zone (submitted to J. Geophys. Res.)

Manuscripts in progress

Dunn, M., H. DeShon, and C. Powell, High-resolution earthquake locations and velocity models in the New Madrid seismic zone (to be submitted to J. Geophys. Res.)

Abstracts

Powell, C. and M. Withers (2008). The effects of Mississippi Embayment Sediments on local earthquake tomography models for the New Madrid seismic zone, Eos Trans. AGU, (89)53, Fall Meet. Suppl., Abstract S43A-1875.

Dunn, M., DeShon, H., and Powell, C. (2008). P and S wave velocity structure and Vp/Vs ratios for the New Madrid seismic zone, Eos Trans. AGU, (89)53, Fall Meet. Suppl., Abstract S43A-1876.

Powell, C. and Withers, M., (2008). The effect of Mississippi Embayment sediments on velocity models determined for the New Madrid seismic zone, *Seism. Res. Lett*., 79, 138.

Powell, C., Dunn, M. and DeShon H. (2009). P- and S-wave velocity structure and Vp/Vs ratios in the New Madrid Seismic zone, USGS Workshop: Meeting of Central and Eastern U.S. Earthquake Hazards Program, Memphis, TN, October 28-29, 28.

DeShon. H., Dunn, M., and Powell, C. (2009). Characterizing near fault velocity structure and seismogenesis along the NewMadrid Seismic Zone, Eos Trans. AGU, (89)53, Fall Meet. Suppl., Abstract S44A-3819.

Powell, C., Withers, M., and DeShon, H. (2009). Intrusions and anomalous Vp/Vs ratios for the New Madrid seismic zone, Eos Trans. AGU, (89)53, Fall Meet. Suppl., Abstract S44A-3809.

REFERENCES

Abers, G.A., and S.W. Roecker (1991), Deep structure of an arc-continent collision: earthquake relocation and inversion for upper mantle P- and S-wave velocities beneath Paupa New Guinea, *J. Geophys. Res., 96*, 6379-6401

Al-Shukri, H., and B. Mitchell, 1988, Reduced seismic velocities in the source zone of the New Madrid Earthquakes, *Bull. Seismol. Soc. Am.,78*, 1491–1509.

Autin, W.J, S.F. Burnes, B.J. Miller, R.T. Saucier, and J.I. Snead (1991), Quaternary geology of the lower Mississippi valley. In: Morrison, R.B. (Ed.), Quaternary

Nonglacial Geology; Conterminous US Geological Society of America, The Geology of North America, Vol. K-2. Boulder, CO, pp. 547-582.
Benz, H. M., B. A. Chouet, P. B. Dawson, J. C. Lahr, R. A. Page, and J. A. Hole (1996), Three-dimensional P and S wave velocity structure of Redoubt Volcano, Alaska, *J. Geophys. Res., 101*, 8111-8128.
Bisrat, S.T, H.R. DeShon, and C.A. Rowe (2008), Swarm activity within the New Madrid seismic zone identified using waveform cross-correlation techniques, 2008. *EOS, Trans. AGU*, *89*(53), Fall Meet. Suppl., Abstract S51C-1757.
Blatt, H. and R.J. Tracy (1997), Petrology (2nd edition, ed.), New York, Freeman: 66 pp.
Bodin, P., K. Smith, S. Horton, and H. Hwang (2001), Microtremor observations of deep sediment resonance in metropolitan Memphis, Tennessee. *Engineering Geology, 62*, 159-168.
Boiron, M.-C., M. Cathelineau, D.A. Banks, B.W.D. Yardley, F. Noronha, and F.M. Miller (1996), P-T-X conditions of late Hercynian fluid penetration and the origin of granite hosted gold quartz veins in northwestern Iberia: a multidisciplinary study of fluid inclusions and their chemistry, *Geochimica et Cosmochimica Acta, 60*, 43-57, doi:10.1016/0016-7037(95)00364-9.
Braile, L.W., G.R. Keller, W.J. Hinze, and E.G. Lidak (1982). An ancient rift complex and its relation to contemporary seismicity in the New Madrid seismic zone, Tectonics, 1, 225-237.
Brown, D., S. Llana-Funez, R. Carbonell, J. Alvarez-Marron, D. Marti, and M. Salisbury (2008), Laboratory measurements of P-wave and S-wave velocities across a surface analog of the continental crust-mantle boundary: Cabo Ortegal, Spain, *Earth Planet. Sci. Lett., 285,* 27-38.
Calais, E., G. Mattioli, C. DeMets, J.-M. Nocquet, S. Stein, A. Newman, and P. Rydelek (2005), Tectonic strain in plate interiors?, *Nature, 438*, doi:10.1038/nature04428.
Catchings, R.D. (1999), Regional Vp, Vs, Vp/Vs and Poisson's ratios across earthquake source zones from Memphis, TN, to St. Louis, MO, *Bull. Seismol. Soc. Am., 89,* 1591-1605.
Chen, K, J.-M. Chiu, and Y. Yang (1996), Shear-wave velocity of the sedimentary basin of the upper Mississippi embayment using S-to-P converted waves, *Bull. Seismol. Soc. Am., 86*, 848-856.
Chen, W.-P., and P. Molnar (1983), Focal depths of intracontinental and intraplate earthquakes and their implications for the thermal and mechanical properties of the lithosphere, *J. Geophys. Res., 88*, 4183-4214.
Cheong, S. (2002), Fluid inclusion study of metamorphic gold-quartz veins in northwestern Nevada, USA: characteristics of tectonically induced fluid, *Geosci. J., 6,* 103-115.
Chevrot, S., and R.D. van der Hilst (2000), The Poisson ratio of the Australian crust: geological and geophysical implications, *Earth Planet. Sci. Lett., 183*, 121-132.
Christensen, N.I. (1989), Pore pressure, seismic velocities, and crustal structure, *Mem. Geol. Soc. Am., 172*, 783-798.
Christensen, N.I. (1996), Poisson's ratio and crustal seismology, *J. Geophys. Res., 101*, 3139-3156.

Christensen, N.I., and W.D. Mooney (1995), Seismic velocity structure and composition of the continental crust: a global view, *J. Geophys. Res., 100*, 9761-9788.

Chiu, J. M., A. C. Johnston, and Y. T. Yang (1992), Imaging the active faults of the central NMSZ Using PANDA Array Data, *Seismol. Res. Lett., 63*, 375-393.

Chiu, J., S. Chiu, and S. Kim, 1997, The significance of the crustal velocity model in local earthquake locations from a case example of a PANDA experiment in the central United States, *Bull. Seismol. Soc. Am.,87*, 1537–1552.

Cox, R., and R. VanArsdale, 2002, The Mississippi Embayment, North America: A first order continental structure generated by the Cretaceous superplume mantle event: *J. Geodyn*., *34*, 163–176.

Crone, A.J. (1981), Sample description and stratigraphic correlation of the New Madrid test well-1-X, New Madrid County, Missouri. *US Geological Survey Open-File Report 81-426*, 26.

Crone, A.J., F.A.McKeown, S.T. Harding, R.M. Hamilton, D.P. Russ, and M.D. Zoback (1985), Structure of the New Madrid seismic source zone in southeastern Missouri and northeastern Arkansas, *Geology, 13*, 547-550, doi:10.1130/0091-7613(1985)13<547:SOTNMS>2.0.CO;2.

Dart, R.L. (1992), Catalog of pre-Cretaceous drill-hole data from the Upper Mississippi embayment: A revision and update of Open File Report 90-260. *US Geological Survey Open-File Report 90-685*, 236.

Dart, R.L. and H.S. Swolfs (1998), Contour mapping of relic structures in the Precambrian basement of the Reelfoot rift, North American midcontinent, *Tectonics, 17*, 235-249.

Dodge, D., G. Beroza, and W. Ellsworth, 1995, Evolution of the 1992 Landers, California, foreshock sequence and its implications for earthquake nucleation, *J. Geophys. Res., 100,* 9865–9880.

Dorman, J., and R. Smalley (1994), Low-frequency seismic surface waves in the upper Mississippi embayment, *Seism. Res. Lett., 65*, 137-148.

Dunn, M. (2009), High resolution earthquake locations and velocity models in the New Madrid seismic zone, Ph.D. Dissertation, The University of Memphis, Memphis, TN, 137pp.

Dvorkin, J., G. Mavko, and A. Nur (1999), Overpressure detection from compressional and shear wave data, *Geophys. Res. Lett., 26*, 3417-3420.

Eberhart-Phillips, D., W. Stanley, B. Rodriguez, and W. Lutter (1995), Surface seismic and electrical methods to detect fluids released due to faulting, J. Geophys. Res., 100, 12919-12936.

Eberhart-Phillips, D., 1990, Three-dimensional P and S velocity structure in the Coalinga region, California, *J. Geophys. Res., 95*, 15343–15363.

Eberhart-Phillips, D., and M. Reyners, 1997, Continental subduction and three-dimensional crustal structure: the northern South Island, New Zealand, *J. Geophys. Res., 102,* 11843–11861.

Ervin, C.P., and L.D. McGinnis (1975), Reelfoot rift – reactivated precursor to the Mississippi embayment, *Geol. Soc. Am. Bull., 86*, 1287-1295.

Forte, A.M., J.X. Mitrovica, R. Moucha, N.A. Simmons, and S.P. Grand (2007), Descent of the ancient Farallon slab drives localized mantle flow below the New Madrid seismic zone, *Geophys. Res. Lett., 34*, doi:10.1029/2006GL027895.

Ginsburg, A., W.D. Mooney, A.W. Walter, W.J. Lutter, and J.H. Healey (1983), Deep structure of northern Mississippi embayment, *Am. Assoc. Pet. Geol. Bull., 67*, 2031-2046.

Gupta, C., and S.W. Roecker (1993). Effects of three-dimensional ray tracing on earthquake locations, focal mechanisms, and velocity structure of the Loma Prieta region, *Seism. Res. Lett.*, *64*, 40.

Hildenbrand, T.G. (1985), Rift structures of the northern Mississippi embayment from the analysis of gravity and magnetic data, *J. Geophys. Res., 90*, 12607-12622.

Hildendrand, T.G., J.G. Rosenbaum, and R.L. Reynolds (1992), High-resolution aeromagnetic study of the New Madrid seismic zone: a preliminary report, *Seismol. Res. Lett., 63,* 209-221.

Hildenbrand, T.G., and J.D. Hendricks (1995), Geophysical setting of the Reelfoot rift and relations between rift structures and the New Madrid seismic zone, *U.S. Geol. Surv. Prof. Paper. 1538-E*, 30pp.

Hildenbrand, T.G., A. Griscom, R.S. Van Schumus, and W. Stuart (1996), Quantitiative investigations of the Missouri gravity low – a possible expression of a large Late Precambrian batholiths intersecting the New Madrid seismic zone, *J. Geophys. Res., 101*, 21921-21942.

Hildenbrand, T.G, Stuart, W.D., and Talwani, P. (2001), Geologic structures related to New Madrid earthquakes near Memphis, Tennessee, based on gravity and magnetic interpretations, *Engineering Geology, 62*, 105-121.

Holbrook, W.S., D. Gajewski, A. Krammer, and C. Prodehl (1988), An interpretation of wide-angle compressional and shear wave data in southwest Germany: Poisson's ratio and petrological implications, *J. Geophys. Res., 93*, 12081-12106.

Horton, S., W.-Y. Kim, and M. Withers, 2005, The 6 June 2003 Bardwell, Kentucky, earthquake sequence: Evidence for the locally perturbed stress field in the mississippi embayment, *Bull. Seism. Soc. Am., 95*, 431–453.

Hough, S.E., J.G. Armbruster, L. Seeber, and J.F. Hough (2000), On the modified Mercalli intensities and magnitudes of the 1811-1812 New Madrid, central U.S. earthquakes, *J. Geophys. Res., 100*, 23839-23864.

Howe, J.R., and T.L. Thompson (1984), Tectonics, sedimentation, and hydrocarbon potential of the Reelfoot rift, *Oil Gas Jour., 82*, 179-190.

Imber, J., R.E. Holdsworth, S.A.F. Smith, S.P. Jefferies, and C. Collettini (2008), Frictional-viscous flow, seismicity and the geology of weak faults: a review and future directions, in C.A.J. Wibberley, W. Kurtz, J. Imber, R.E. Holdsworth, C. Collettini, eds., The internal structure of fault zones: implications for mechanical and fluid-flow properties, *Geol. Soc. Spec. Pub. 299*.

Jia, Y., and R. Kerrich (2000), Giant quartz vein systems in accretionary orogenic belts: the evidence for a metamorphic fluid origin from $\delta^{15}N$ and $\delta^{13}C$ studies, *Earth Planet. Sci. Lett., 184*, 211-224.

Johnson, G., 2008, Using Earthquake Focal Mechanisms to Investigate Seismotectonics in New Madrid Seismic Zone: Master's thesis, University of Memphis.

Johnston, A.C., and E.S. Schweig (1996), The enigma of the New Madrid earthquakes of 1811-1812, *Annual Rev. Earth Planet. Sci., 24*, 339-384.

Julian, B.R., A. Ross, G.R. Foulger, and J.R. Evans (1996), Three-dimensional seismic image of a geothermal reservoir: The Geysers, California, *Geoph. Res. Lett., 23*, 685-688.

Julian, B.R., A.R. Pitt, and G.R. Foulger (1998), Seismic image of a CO_2 reservoir beneath a seismically active volcano, *Geophys. J. Int., 133*, F7-F10.

Kane, M.F., T.G. Hildenbrand, and J.D. Hendricks (1981), Model for the tectonic evolution of the Mississippi Embayment and its contemporary seismicity, *Geology, 9*, 563-568.

Kenner, S.J., and P. Segall (2000), A mechanical model for intraplate earthquakes: application to the New Madrid seismic zone, *Science, 289*, 2329-2332.

Kerrich, R., and R. Feng (1992), Archean geodynamics and the Abitibi-Pontiac collision: implications for advection of fluids at transpressive collisional boundaries and the origin of giant quartz veins, *Earth Sci. Rev. 32*, 33-60.

Kissling, E., W. Ellsworth, D. Eberhart-Phillips, and U. Kradolfer, 1994, Initial reference models in local earthquake tomography, *J. Geophys. Res., 99*, 19635–19646.

Langston, C.A. (2003a), Local earthquake wave propagation through Mississippi embayment sediments, Part I: body-wave phases and local site responses, *Bull. Seismol. Soc. Am., 93*, 2664-2684.

Langston, C. A (2003b), Local earthquake wave propagation through Mississippi embayment sediments, Part II: influence of local site velocity structure on Qp-Qs, *Bull. Seismol. Soc. Am., 93*, 2685-2702.

Langston, C.A., S.-C. C. Chiu, Z. Lawrence, P. Bodin, and S. Horton (2009a), Array observations of microseismic noise and the nature of H/V in the Mississippi embayment, *Bull. Seism. Soc. Am., 99*, doi:10.1785/0120080189.

Langston, C.A., D. M. Rieger, M. B. Magnani (2009b), Unusual microseisms seen in the Reelfoot fault zone, Northern Tennessee, from a reflection experiment, *Bull.Seism.Soc.Am,* (in press).

Lees, J. M., and P. E. Malin (1990). Tomographic images of P-wave velocity variation at Parkfield, California, *J. Geophys. Res., 95*, 21793-21804.

Liu, L., M. Zoback, and P. Segall, 1992, Rapid intraplate strain accumulation in the New Madrid seismic zone : Science, 257, 1666–1669.

Marcher, M.V., and R.G. Stearns (1962), Tuscaloosa formation in Tennessee, *Geol. Soc. Am. Bull., 73*, 1365-1386, DOI:10.1130/0016-7606(1962)73[1365:TFIT]2.0.CO;2.

Mark, G., P.J. Williams, and A.J. Boyce (2004), Low latitude meteoric fluid flow along the Cloncurry fault, Cloncurry District, NW Queensland, Australia: geodynamic and metallogenic implications, *Chem. Geol., 207*, 117-132.

Meissner, R., and J. Strehlau (1982), Limits of stresses in continental crusts and their relation to the depth-frequency distribution of shallow earthquakes, *Tectonics, 1*, 73-89.

McCaig, A.M. (1988), Deep fluid circulation in fault zones, *Geology, 16*, 867-870, doi:10.1130/0091-7613(1988)016<0867:DFCIFZ>2.3.CO;2.

McCaig, A.M., J. Tritlla, and D.A. Banks (2000), Fluid mixing and recycling during Pyrenean thrusting: evidence from fluid inclusion halogen ratios, *Geochimica et Cosmochimica Acta, 64,* 3395-3412.

McKeown, F.A., and S.F. Diehl (1994), Evidence of contemporary and ancient excess fluid pressure in the New Madrid seismic zone of the Reelfoot rift, central United States, in Investigations of the New Madrid Seismic Zone, *U.S. Geol. Surv. Prof. Pap. 1538-N*, ed. K.M. Shedlock, A.C. Johnston, pp. N1-N24.

McKeown, F.A., R.M. Hamilton, S.F. Diehl, and E.E. Glick (1990), Diapiric origin of the Blytheville and Pascola arches in the Reelfoot rift, east-central United States: relation to New Madrid seismicity, *Bull. Geol. Soc. Am., 18*, 1158-1162, doi: 10.1130/0091-7613(1990)018<1158:DOOTBA>2.3.CO;2.

Michelini, A., and T.V. McEvilly (1991), Seismological studies at Parkfield I: simultaneous inversion for velocity structure and hypocenters using B-splines parameterization, *Bull. Seism. Soc. Am., 81*, 524-552.

Miller, S., A. Nur, and D. Olgaard, 1996, Earthquakes as a coupled shear stress-high pore pressure dynamical system, *Geophys. Res. Lett., 23*, 197–200.

Mooney, W.D., and M.C. Andrews (1984), Seismic refraction studies of the Mississippi embayment, in Proceedings of the Symposium on the New Madrid Seismic Zone, *U.S. Geol. Surv. Open File Rept., 84-770*, 138-167.

Mooney, W.D., M.C. Andrews, A. Ginsburg, D.A. Peters, and R.M. Hamilton (1983), Crustal structure of the northern Mississippi embayment and a comparison with other continental rift zones, *Tectonophysics, 94*, 327-348.

Moos, D., and M. Zoback, 1983, In situ studies of velocity in fractured crystalline rock, *J. Geophys. Res., 88,* 2345–2358.

Moretti, M., P. DeGori, and C. Chiarabba (2009), Earthquake relocation and three-dimensional Vp and Vp/Vs models along the low angle Alto Tiberina fault (central Italy): evidence for fluid overpressure, *Geophys. J. Int., 176*, 833-846.

Nakajima, J., T. Matsuzawa, A. Hasegawa, and D. Zhao, 2001. Three-dimensional structure Vp, Vs, and Vp/Vs beneath northeastern Japan: implications for arc magmatism and fluids, Jour. Geophys. Res., 106, 21843-21857.

Nelson, K.D., and J. Zhang (1991), A COCORP deep reflection profile across the buried Reelfoot rift, south-central United States, *Tectonophysics, 197*, 271-293.

Newman, A., S. Stein, J. Weber, J. Engeln, A. Mao, and T. Dixon (1999), Slow seismic deformation and lower seismic hazard at the New Madrid seismic zone, *Science, 284*, 619-621.

Nur, A., and G. Simmons, 1969, The effect of saturation on velocity in low porosity rocks, *Earth Planet. Sci. Lett., 7,* 183–193.

O'Connell, R.J., and B. Budiansky (1974), Seismic velocity in dry and saturated cracked solids, *J. Geoph. Res., 78*, 5412-5426.

Odum, J., W. Stephenson, K. Shedlock, and T. Pratt, 1999, Near-surface structural model for deformation associated with the February 7, 1812, New Madrid, Missouri, earthquake, *Geol. Soc. Am. Bull., 110*, 149–162.

Parrish, S., and R. VanArsdale, 2004, Faulting along the southeastern margin of the Reelfoot rift in northwestern Tennessee revealed in deep seismic reflection profiles, *Seism. Res. Lett., 75*, 782–791.

Paige, C.C., and M.A. Saunders (1982), LSQR: an algorithm for sparse linear equations and sparse least squares, *ACM Trans. Math. Software, 8*, 43-71.

Pollitz, F., L. Kellogg, and R. Burgmann, 2001, Sinking mafic body in a reactivated lower crust: A mechanism for stress concentration at the New Madrid seismic zone, *Bull. Seism. Soc. Am., 91*, 1882–1897.

Powell, C.A., and M. Withers (2009), The effects of Mississippi embayment sediments on local earthquake tomography, *Seism. Res. Lett., 80*, 149-158.

Podvin, P., and I. Lecomte (1991), Finite difference computation of travel-times in very contrasted velocity models: A massively parallel approach and its associated tools, *Geophys. J. Int., 105*, 271-284.

Pujol, J. (2006), Effect of the unconsolidated sediments in the New Madrid seismic zone on the 3-D velocity models derived from inversion of arrival times, *Seismol. Res. Lett., 77*, 102.

Pujol, J., A. Johnston, J.-M. Chiu, and Y. Yang (1997), Refinement of thrust faulting models for the central New Madrid seismic zone, *Engineering Geology, 46*, 281-298.

Rabak, I (2009), Crustal structure of the Reelfoot rift, Ph.D. Dissertation, the University of Memphis, Memphis, TN, 138pp.

Ravat, D.N., Braile, L.W. and Hinze, W.J. (1987), Earthquakes and plutons in the midcontinent – evidence from the Bloomfield pluton, New Madrid rift complex, *Seismol. Res. Lett., 58*, 41-52.

Reyners, M., D. Eberhart-Phillips, and G. Stuart, 1999, A three-dimensional image of shallow subduction: crustal structure of the Raukumara Peninsula, New Zealand, *Geop. J. Int., 137*, 873–890.

Romero, S., and G.J. Rix (2001), Regional variations in near surface shear wave velocity in the Greater Memphis area, Engineering *Geology, 62*, 137-158.

Russ, D.P. (1982), Style and significance of surface deformation in the vicinity of New Madrid, Missouri: investigations of the New Madrid, Missouri, earthquake region, *Geol. Surv. Prof. Paper 1236*, 95-114.

Schweig, E., and M. Ellis, 1994, Reconciling short recurrence intervals with minor deformation in the New Madrid Seismic Zone, *Science, 264*, 1308–1309.

Smalley, R., M.A. Ellis, J. Paul, and R.B. VanArsdale (2005), Space geodetic evidence for rapid strain rates in the New Madrid seismic zone of central USA. *Nature*, doi:10.1038/nature03642.

Stearns, R.G., and M.V. Marcher (1962). Late Cretaceous and subsequent structural development of the northern Mississippi embayment area, Geol. Soc. Am. Bull., 73, 1387-1394.

Stein, S. (2007), New Madrid GPS: Much ado about nothing? *Forum, EOS Trans. AGU, 80*, 59.

Stephenson, W.J., J.K. Odum, R.A. Williams, T.L. Pratt, R.W. Harrison, and D. Hoffman (1999), Deformation and Quaternary faulting in southeast Missouri across the Commerce geophysical lineament, *Bull. Seism. Soc. Am., 89*, 140-155.

Stibson, R.H. (1994), Deformation and fluid flow: crustal stress, faulting and fluid flow, *Geol. Soc. London, special Publications, 78*, 69-84.

Takei, Y. (2002), Effect of pore geometry on Vp/Vs: from equilibrium geometry to crack, *J. Geophys. Res., 107*, doi:10.1029/2001JB000522.

Thomas, W.A. (1985), Northern Alabama sections, in Woodward, N.B., ed., Valley and Ridge thrust belt: balanced structural sections, Pennsylvania to Alabama (Appalachian Basin Industrial Associates): University of Tennessee Department of Geological Sciences Studies in Geology 12, p. 54-61.

Thomas, W.A. (1991), The Appalachian-Ouachita rifted margin of southeastern North America. *Geol. Soc. Am. Bull., 103*, 415-431, doi: 10.1130/0016-7606(1991)103<0415:TAORMO>2.3.CO;2.

Thurber, C., S. Roecker, K. Roberts, M. Gold, L. Powell, and K. Rittger (2003), Earthquake locations and three-dimensional fault zone structure along the creeping section of the San Andreas fault near Parkfield, CA: preparing for SAFOD, *J. Geophys. Res., 30*, 1112, doi:10.1029/2002GL016004.

Thurber, C., 1983, Earthquake locations and three-dimensional crustal structure in the Coyote Lake area, central California, *J. Geopys. Res., 88*, 8226–8236.

Thurber, C., T. Brocher, H. Zhang, and V. Langenheim, 2007, Three Dimensional P wave model for the San Francisco Bay region, California, *J. Geopys. Res.,112*.

Tryggvason, A., S. Th. Rögnvaldsson, and Ó. G. Flóvenz (2002), Three dimensional imaging of the P- and S-wave velocity structure and earthquake locations beneath southwest Iceland. *Geophys. J. Int.*, 151, pp. 848-866, doi:10.1046/j.1365-246X.2002.01812.x.

Tuttle, M.P. (2001), The use of liquefaction features in paleoseismology: lessons learned in the NMSZ, central United States, *J. Seismol., 5*, 361-380.

Tuttle, M.P., E.S. Schweig III, J. Campbell, P.M. Thomas, J.D.Sims, and R.H. Lafferty III (2005), Evidence for New Madrid earthquakes in A.D. 300 and 2350 B.C. at the Burkett archeological site, *Seism. Res. Lett., 76*, 489-501.

VanArsdale, R., R. Bresnahan, N. McCallister, and B. Waldron, 2007, Upland Complex of the central Mississippi River valley: Its origin, denudation, and possible role in reactivation of the New Madrid seismic zone, *Geol. Soc. Am. special paper, 425*, 177–192.

VanArsdale, R.B., and R.K. TenBrink (2000). Late Cretaceous and Cenozoic geology of the New Madrid Seismic Zone. Bulletin of the Seismological Society of America, 90, 345-356.

Van der Pluijm, B.A., and P.A. Catacosinos (1996), Basement and basins of eastern North America, Geological Society of America Special Paper 308, 205 pp.

Vlahovic, G. and Powell, C. A., 2001. Three Dimensional S-Wave Velocity structure and Vp/VS ratios in the New Madrid seismic zone, *J.Geophys. Res.* , *106*, 13501-13514.

Vlahovic, G., Powell, C., and J-M Chiu (2000), Three-dimensional P-wave velocity structure in the New Madrid seismic zone based upon PANDA arrival time data, *J. Geophys. Res*., *105*, 7999-8012.

Waldhauser, F., 2001, hypoDD: a computer program to compute double-difference hypocenter locations, *U.S. Geol. Surv. Open-File Report, 25*, 1–113.

Waldhauser, F., and W. L. Ellsworth, 2000, A double-difference earthquake location algorithm, Method and application to the northern Hayward Fault, California, *Bull. Seism. Soc. Am., 90,* 1,353–1,368.

White, D.J., B. Milkereit, M.H. Salisbury, and J.A. Percival (1992), Crystalline lithology across the Kapuskasing uplift determined using in situ Poisson's ratio from seismic tomography, *J. Geophys. Res., 97*, 19993-20006.

Wibberley, C.A.J., G. Yielding, and G. Di Toro (2008), Recent advances in the understanding of fault zone internal structure: a review, in C.A.J. Wibberley, W. Kurtz, J. Imber, R.E. Holdsworth, C. Collettini, eds., The internal structure of fault zones: implications for mechanical and fluid-flow properties, *Geol. Soc. Special Publication 299.*

Wilkens, R., G. Simmons, and L. Caruso, 1984, The ratio Vp/Vs as a discriminant of composition for siliceous limestones, *Geophys., 49,* 1850–1860.

Wolf, L.W., M.-K. Lee, S. Browning, and M.P. Tuttle (2005), Numerical analysis of overpressure development in the New Madrid seismic zone, *Bull. Seism. Soc. Am., 95,* 135-144.

Xie, J. (2001), Rupture characteristics of clustered microearthquakes and variations in fault properties in the New Madrid seismic zone, *J. Geophys. Res., 106*, 26495-26509.

Xie, J., Z. Liu, L. Cong, R.B. Herrmann, and J.-M. Chiu (1997), Rupture properties of clustered microearthquakes near intersecting faults of the New Madrid seismic zone: implications for fault weakening, *J. Geophys. Res., 102*, 8187-8202.

Yonkee, W.A, W.T. Parry, and R.L. Bruhn (2003), Relations between progressive deformation and fluid-rock interaction during shear-zone growth in a basement-cored thrust sheet, Sevier orogenic belt, Utah, *Am. J. Sci., 303*, 1-59, doi:10.2475/ajs.303.1.1.

Zhang, H., 2003, Double-difference seismic tomography method and its applications: PhD thesis, University of Wisconsin-Madison.

Zhang, H., and C. H. Thurber (2003), Double-difference tomography: The method and its application to the Hayward Fault, California, Bull. *Seismol. Soc. Am., 93,* 1875-1889.

Zhang, Z., X. Zhang, and J. Badal (2008), Composition of the crust beneath southeastern China derived from an integrated geophysical data set, *J. Geophys. Res., 113*, B04417, doi:10.1029/2006JB004503.

Zhang, Q., Sandvol, E., and M. Liu (2009), Lithospheric velocity structure of the New Madrid seismic zone: a joint teleseismic and local P tomographic study, *Geop. Res. Lett.*, *36*, L11305, doi:10.1029/2009GL037687.

Zhao, D., H. Kanamori, H. Negishi, and D. Wiens, 1996, Tomography of the source area of the 1995 Kobe Earthquake: Evidence for fluids at the hypocenter?, *Science, 274*, 1891–1894.

Zhao, D., and H. Negishi (1998), The 1995 Kobe earthquake: seismic image of the source zone and its implications for the rupture nucleation, *J. Geophys. Res., 103*, 9967-9986.

Zhao, D., O.P. Mishra, and R. Sanda (2002), Influence of fluids and magma on earthquakes: seismological evidence, *Phys. Earth Planet. Int., 132*, 249-267.

Zhao, D. and Li, J., A. Hasegawa and S. Horiuchi (1992), Tomographic imaging of P and S wave velocity structure beneath northeastern Japan, *J. Geophys. Res.* ***97***, 19909–19928.